Department of Physics and Astronomy
University of Heidelberg

Master thesis
in Physics
submitted by
Ilja Zebergs
born in Tallinn, Estonia
2023

TrapREMI as a Tool for Investigating Ion-Atom Collisions

This Master thesis has been carried out by

Ilja Zebergs

at the

Max Planck Insitute for Nuclear Physics

under the supervision of

Priv.-Doz. Dr. Robert Moshammer

TrapREMI as a Tool for Investigating Ion-Atom Collisions

The TrapREMI is a setup combining an electrostatic ion beam trap (EIBT) with a reaction microscope (REMI) to study the dynamics of (molecular) ions and charged clusters. Ions are stored in the EIBT in a linear oscillatory motion at some keV. The EIBT enables ion beam preparation, including e.g. limiting the transversal momentum as well as allowing mass analysis and selection. Inside the REMI the ion beam is crossed with a target/projectile beam and the resulting reaction products are detected with time- and position-sensitive detectors. This allows reconstruction of their 3D-momenta. Ions, neutral atoms/molecules and electrons can be detected in coincidence. This thesis focuses on the implementation of the ion-atom collision experiments in the TrapREMI. For this purpose a supersonic gas jet setup was built to provide a cold gas beam as a target. Afterwards, the first proof-of-principle experiment was conducted: A singly-charged argon ion captures an electron from a neutral argon atom and both particles are detected in coincidence. Additionally, a new ion source was installed, voltage control was modified for a simpler operation and a technique for ion bunch creation inside the EIBT was briefly tested.

TrapREMI als Instrument zum Untersuchen der Ion-Atom Stöße

TrapREMI ist ein Aufbau, der eine elektrostatische Ionenfalle mit einem Reaktionsmikroskop (REMI) kombiniert, um die Dynamik von (molekularen) Ionen und geladenen Clustern zu untersuchen. Ionen werden in einer oszillatorischen Bewegung entlang einer Achse mit kinetischer Energie von einigen keV gespeichert. Die Ionenfalle ermöglicht z.B. Einschränkung des transversalen Impulses sowie Massenanalyse und -selektion. Innerhalb des REMI wird der Ionenstrahl mit einem Target-/Projektilstrahl gekreuzt und die Reaktionsprodukte werden mit zeit- und positionssensitiven Detektoren erfasst. Dies ermöglicht die Rekonstruktion ihrer 3D-Impulse. Ionen, neutrale Atome/Moleküle und Elektronen können in Koinzidenz detektiert werden. Diese Arbeit konzentriert sich auf die Implementierung von Ion-Atom Stoßexperimenten im TrapREMI. Zu diesem Zweck wurde ein Gasjet aufgebaut, der einen kalten Gasstrahl als Target bereitstellt. Anschließend wurde das erste Test-Experiment durchgeführt: Ein einfach geladenes Argon-Ion fängt ein Elektron von einem neutralen Argon-Atom ein, und beide finalen Teilchen werden in Koinzidenz detektiert. Zusätzlich wurde eine neue Ionenquelle installiert, die Spannungssteuerung wurde modifiziert für eine einfachere Bedienung und eine Technik zur Erzeugung von Ionenbündeln in der Falle wurde kurz getestet.

Introduction

TrapREMI is a recently developed device, built to investigate dynamics of (molecular) ions and charged clusters in (photo-)chemical reactions [26]. The setup combines an electrostatic ion beam trap (EIBT) with a reaction microscope (REMI). An EIBT stores ions in an oscillating motion along a single axis using an electrostatic potential [36]. The EIBT limits the transversal momentum distributions and enables ion beam preparation techniques, e.g. mass spectrometry [37] and selection [30], longitudinal ion beam compression into a bunch [6] or longitudinal cooling [7]. A REMI allows 3D-momentum imaging of reaction products in kinematically complete measurements with up to 4π solid angle acceptance [13]. The TrapREMI distinguishes itself from similar experiments through the possibility for more complex detection schemes via simultaneous detection of ions, neutral atoms/molecules as well as electrons in coincidence. Note that most of the existing experiments using a REMI or a similar fragment momentum mapping technique can only detect at maximum two of these three fragment types. The TrapREMI device can in principle be connected to any target/projectile source in a straightforward manner in order to induce reactions of interest. Together with the table-top nature of the setup this allows for a large versatility in the choice of the subject to be investigated. Previously it was connected to an IR-laser for the first test experiments with the REMI: photo-dissociation of stored molecular ions [27].

This work focuses mainly on the implementation of collision experiments between ions and neutral atoms/molecules in the TrapREMI setup. It is of great interest to understand such reactions in more detail as they play an important role in gas-phase chemistry in different environments, e.g. chemistry of Earth's ionosphere [17] or complex molecule formation pathways in the interstellar medium [15].

Different ion-atom collision experiments were already conducted in the past. In the following, some examples are given: Different collisions with highly-charged ions have been studied in REMI, e.g. [14]. Young-type interference of a recoil ion could be observed in the dissociative electron capture by a diatomic molecular ion from an atom using cold

target recoil ion momentum spectroscopy (similar to REMI) [24]. There was also recent progress in using ion-atom collisions in order to create ultra-cold ions from a cooled atom cloud via symmetric charge-exchange in the so-called swap cooling [12].

To enable ion-atom collision experiments in the TrapREMI a supersonic gas jet setup was assembled and connected to the pre-existing setup. The jet provides a target of neutral gas particles. A cold directed beam is created via expansion from a high pressure reservoir into a vacuum chamber through a microscopic nozzle.

Afterwards the overall conduction of ion-atom collision experiments in the TrapREMI setup was tested in a simple charge-exchange experiment. A singly-charged argon ion captures an electron from a neutral argon atom and both final particles are detected on separate time- and position-sensitive detectors in coincidence. Argon dimers are produced in the jet due to cooling and can be observed in the experimental data. Besides the dominant argon isotope ^{40}Ar we recognize the lighter and far less abundant isotopes ^{36}Ar and ^{38}Ar in both the ion beam and the jet.

Additionally, some modifications have been done to the setup: A new ion source was installed, and control of the electrode voltages via a PC software was implemented. A technique for longitudinal compression of the ion beam into a short pulse from inside the EIBT was briefly tested in this work as well.

This thesis is divided into four chapters: Chapter 1 gives an overview of the setup, main instruments and their operation. Chapter 2 describes the functioning principle of a supersonic gas jet, as well as the design and the assembly process of the jet setup for the TrapREMI. Chapter 3 describes how the ion-atom collision experiment was performed and reports the results. It also summarizes some insight/recommendations that might be useful for future experiments. Chapter 4 describes the ion bunching technique and the results of a short test thereof in TrapREMI. Finally, Chapter 5 summarizes the thesis.

Contents

1 TrapREMI experimental setup

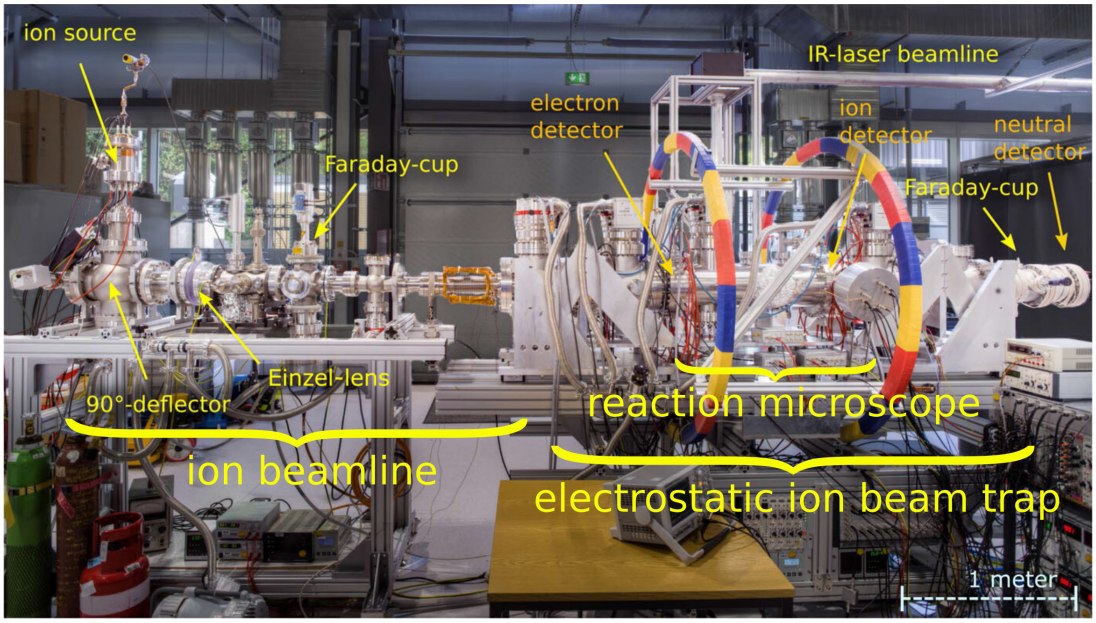

Figure 1: TrapREMI setup photo, modified from [27].
(The laser beamline was disconnected during this thesis.)

This chapter gives an overview of the pre-existing TrapREMI setup, as shown in Fig. 1. An ion source produces ions that are injected into an electrostatic ion beam trap (EIBT) where they are stored in motion at several keV. Inside the EIBT reactions are induced by crossing the ion beam with a projectile/target beam, e.g. a laser as in Fig. 1. Those reactions can be observed using a reaction microscope, which is integrated into the EIBT. Following sections describe the mentioned instruments as well as the possibilities they provide: Section 1.1 showcases the EIBT, Section 1.2 the REMI and Section 1.3 the ion beam production. Finally, an overview of the setup operation is given in Section 1.4.

A more detailed description of the pre-existing setup, its assembly, operation, characterization as well as the first proof-of-principle experiments (photo-dissociation of molecular ions) can be found in the PhD thesis of F. Schotsch [26]. A more compact overview of the setup was also published [27].

1.1 Electrostatic ion beam trap

An electrostatic ion beam trap (EIBT) is a device for storing an ion beam at motion in a fully electrostatic potential [36]. An EIBT can be seen as a simpler and more compact alternative to electrostatic storage rings, allowing similar ion beam preparation and analysis techniques [22]. The ions are confined to a linear oscillating motion between two electric potential ramps (electrostatic mirrors), similar to light confined between two mirrors in an optical resonator. The storage energy, i.e. the maximal kinetic energy of the ions in an EIBT, is typically of a few keV per charge number. Thus typical oscillation periods for singly-charged ions with masses of a few 10 u in an order 1 m long EIBT are of the order of 10 µs. An EIBT can store ions at room temperature for up to a few seconds [37].

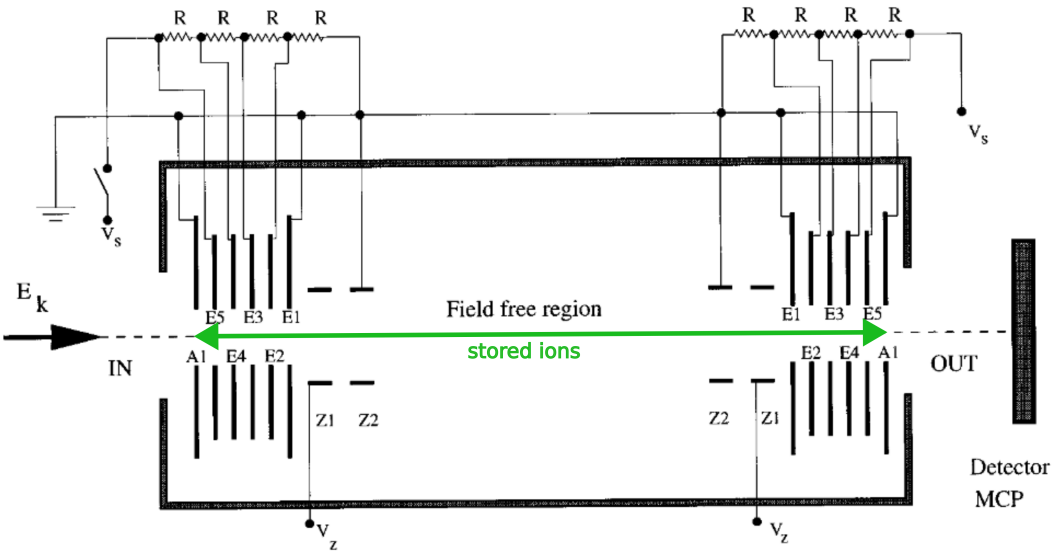

Figure 2: Scheme of the first EIBT, modified from [36].

The typical electrode geometry of an EIBT can be seen in Fig.2 [36]. In order for ions to pass through the electrodes and to preserve cylindrical symmetry of the electric field along the oscillation axis, cylindrical electrodes are used. The mirrors are realized by several electrodes in a row connected to a high voltage via a voltage divider (E1 - E5 in Fig. 2). When the potentials are high enough, the ion beam is confined longitudinally, oscillating between the two mirrors.

While the mirrors introduce some transversal focusing, the effect is mostly too weak to confine the ions in the transversal direction. To solve this, an additional focusing element, the so-called einzel lens, is introduced in front of the either mirror. An einzel lens consists of three cylindrically symmetric electrodes in a row (E1, Z1, Z2 in Fig.2): the middle electrode (Z1) is kept at high potential, both outer electrodes (E1, Z2) are kept at lower potential. This creates a potential bump along the ion movement axis. The exact resulting potential can be found by solving the Laplace equation for the electrostatic potential: $\nabla^2 V = 0$ with boundary conditions given by the electrode voltages. One obtains a potential similar to that illustrated in Fig. 3. Inside the middle electrode, the potential is monotonically increasing when moving from the center axis to the electrode surface. This creates a focusing effect for the ions passing through it. In both spaces between the middle electrode and the either neighboring electrode the ion beam diverges. The overall effect is however focusing, because the beam is focused at a higher potential and thus a lower velocity. The exact dynamics of the ion beam needs to be simulated or experimentally determined for a given electrode geometry, potentials and the velocity and spatial distribution of the ion beam.

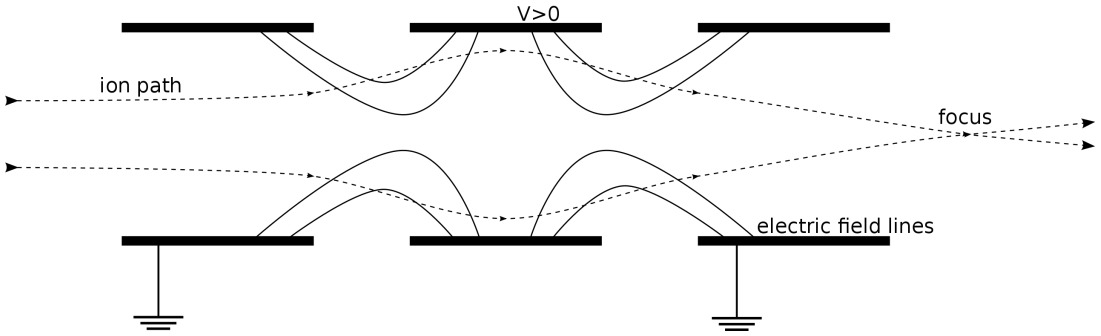

Figure 3: Schematic drawing of an einzel lens, electric field lines therein and exemplary ion trajectories, source: [1].

The storage conditions in an EIBT do not depend on the ion mass due to its electrostatic nature, meaning there is in principle no upper limit for the mass of the stored particles. Even charged nanoparticles with masses in the order of several 10^8 u have been successfully stored in an EIBT [9]. This also allows simultaneous storage of ions of different masses. The only mass limitations may arise due to the effects of unwanted magnetic fields (mostly the Earth's magnetic field) for very low masses [26].

For a periodic motion of a charged particle inside an electrostatic potential the period is proportional to the square-root of the mass-to-charge ratio:

$$T \propto \sqrt{\frac{m}{q}} \ . \tag{1}$$

This makes an EIBT suitable as a time-of-flight (ToF) mass spectrometer, as long as the ion beam can be pulsed and the relative charge density can be measured at one point along the trap axis [37]. It can be also used to select certain ion masses for a further storage and discard the others using mass kick-out technique [30] (potential use in the TrapREMI briefly discussed in Section 3.4.3).

For the full description of the ion beam dynamics one needs to include the repulsive Coulomb force between the ions. The effect is negligible for low ion densities, however it can be observed at higher densities, especially in the reverse points inside the mirrors where the velocities are the lowest and thus the beam is longitudinally compressed. While the Coulomb force introduces some upper limit for the number of the stored ions, it can be useful for certain ion beam preparation techniques e.g. self-bunching for storing non-dispersive ion bunches [18] or autoresonance cooling [7] for a narrower longitudinal velocity distribution.

EIBT in TrapREMI

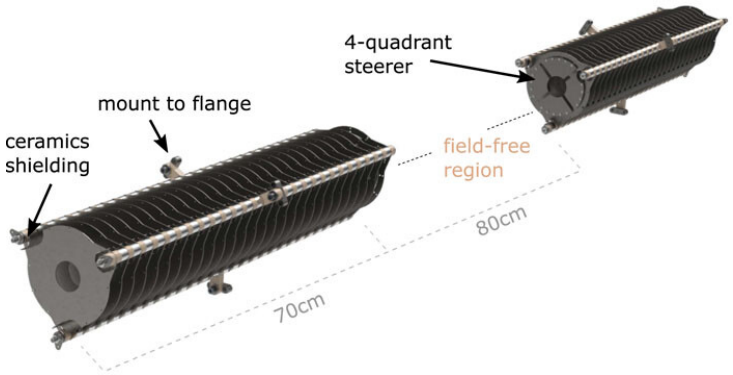

Figure 4: EIBT electrode stacks in TrapREMI, source: [27].

The EIBT in TrapREMI consists of two stacks of 26 identical electrodes coaxially opposing each other, as illustrated in Fig. 4. The cylindrical electrodes have an inner diameter of 40 mm, an outer diameter of 154 mm and a thickness of 1 mm. The spacing between the electrodes is 25 mm. The voltage of each electrode can be separately controlled. An electrostatic mirror and an einzel lens are implemented in either stack by connecting power supplies to certain electrodes, as shown in Appendix A. The positions of the elements as well as the spatial length of the mirrors can be varied. At the inner end of the either stack a 4-quadrant-steerer (4 separate cylinder quadrant electrodes) is implemented. It can steer the ion beam with a transversal electric field to compensate for the possible misalignment between the two stacks or between the ion beamline and the EIBT.

In the middle of the trap is a region with no EIBT electrodes. This region is where the reactions take place and the reaction microscope is implemented. Here the ions move along the trap axis with a well-defined velocity. The rather large dimensions of the EIBT were chosen in order to accommodate the reaction microscope between the EIBT stacks.

1.2 Reaction microscope

Basic design and working principle

A reaction microscope (REMI) is a tool for 3D-momentum imaging of reaction products with a possibility of 4π solid angle acceptance [13]. The reader can find an overview of some benchmark experiments conducted using a REMI in [25], including e.g. Q-value measurements in ion-atom collisions [14], molecular structure imaging [19], vibrational wavefunction imaging [23] and time-resolved dynamics using pump-probe laser technique [3].

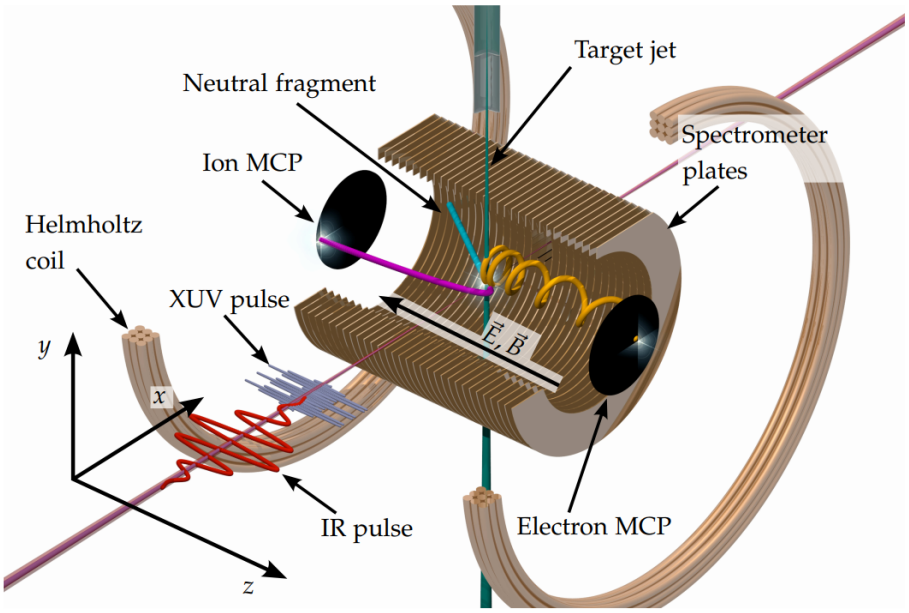

Figure 5: Typical REMI design and working principle, source: [2].

A typical design can be seen in Fig. 5. A reaction is induced in the middle of the REMI by crossing two beams, e.g. a gas jet is crossed with a laser. A homogeneous electric field is created with a stack of cylindrical electrodes ("spectrometer plates" in Fig. 5) and a homogeneous magnetic field is generated parallel to it using a Helmholtz coil.

The positive ions produced in the reaction are accelerated along the electric field onto a time- and position-sensitive detector (labelled "ion MCP" in Fig. 5). A typical choice for such a detector is a multi-channel plate (MCP) combined with delay lines. The 3D-

momentum of the ion directly after the reaction can be reconstructed from the position of the hit and the ions' travel time. By choosing a sufficiently strong electric field ions of any momentum can be extracted onto the detector. Higher electric field however reduces the momentum resolution. Thus a suitable electric field strength should be chosen to balance between the acceptance and the resolution.

Electrons are accelerated in the opposite direction towards another time- and position sensitive detector (labelled "electron MCP" in Fig. 5). However, the electric field suitable for the ions is typically not sufficient to extract all the electrons onto the detector due to their low mass. An additional magnetic field keeps the electrons on a cyclotron trajectory with the radius smaller than half of the detector radius and therefore be able to detect them. Their 3D-momenta can be reconstructed by additionally taking the cyclotron movement into account. The cyclotron frequency of the ions is very low and the cyclotron radius very large due to their significantly higher mass, thus the influence of the magnetic field on their trajectory can be neglected.

Negative ions can be detected in analogy to the positive ones but on the electron detector. Neutral fragments can only be detected in this configuration if they fly directly towards one of the detectors with high enough kinetic energy to activate the MCP, which is highly unlikely.

MCP and delay line detector

An MCP is an array of small electron-multiplier tubes [35], as depicted in Fig. 6. It is a solid piece of highly-resistive material, typically glass, with a large number of small (usually of several 10µm) tunnels (channels). Either face of an MCP is electroded (coated with a layer of conductive material). When a high voltage (some keV) is applied across an MCP, the walls of the channels eject electrons on impact. The strong electric field arising immediately in front of an MCP accelerates either positively or negatively charged particles (depending on the configuration of the MCP voltages) towards the channel walls causing an electron avalanche resulting in a detectable electron cloud behind the detector.

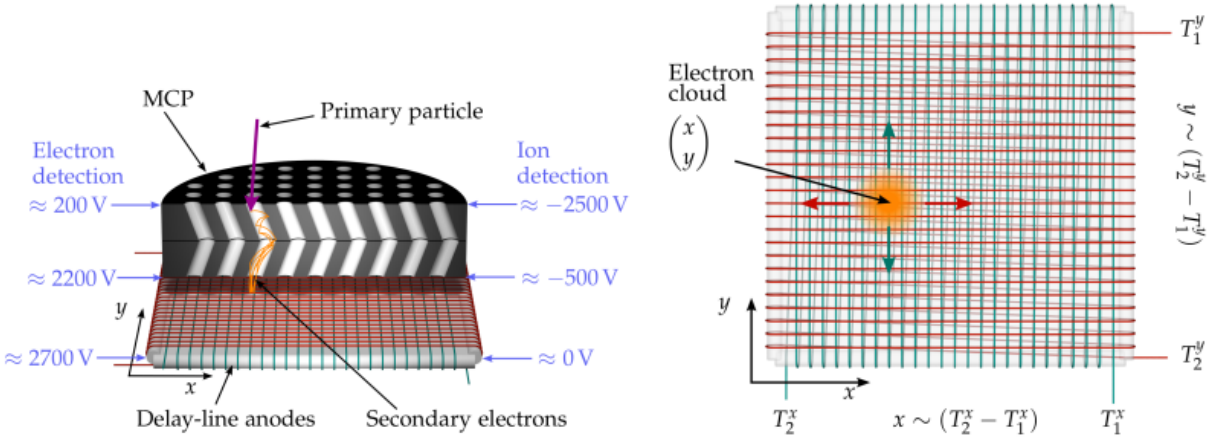

Figure 6: MCP & delay line detector working principle. Left: MCP with typical potentials. Right: hit position reconstruction with delay lines. Adapted from [2].

Particles with opposite charge get reflected and thus cannot be detected. Neutral particles can only be detected if they originally move towards the detector with a high enough kinetic energy. Due to the fact that the MCP area is only partially covered by the channels, detection efficiency is less than unity.

The time of a hit can be measured through the voltage drop across the MCP due to the emerging electron cloud. The electron cloud from the MCP impinges on the delay lines. A delay line is a low resistance wire wound around a frame along one direction with equal distance between the windings (see green or red wire in Fig.6 on the right). The electron cloud hitting this wire causes a voltage signal travelling in both directions along the wire. The difference between the arrival times on either end of the wire is proportional to the position of the electron cloud along the winding direction. Using two crossed delay lines one can determine the 2D-position on the detector from the four arrival times of the signal.

In order to mitigate the ambient noise, each delay-line wire is implemented doubly, consisting of a signal wire and a reference wire near it. Both wires are identically capacitively coupled to the environment and thus experience the same induced noise. The signal wire is held on a slightly higher potential, such that the electron cloud is drawn to it but not the reference wire. Subtracting the reference from the signal compensates for the induced noise, thus enhancing the signal-to-noise ratio.

Integration of the REMI into the EIBT

TrapREMI setup uses a reaction microscope in a slightly different configuration to enable detection of the neutral fragments. It is located between the two EIBT stacks and the ion beam passes through along the axis of the REMI (parallel to the electric and the magnetic field) (see Fig.7). This requires holes in the middle of the REMI detectors. In the REMI the ion beam is crossed with a target/projectile beam. We refer to the detector on the side of the ion beamline as the "front detector" and the other detector inside the REMI as the "rear detector". An additional MCP detector is implemented behind the REMI outside of the EIBT to detect neutral fragments (further called "neutral detector").

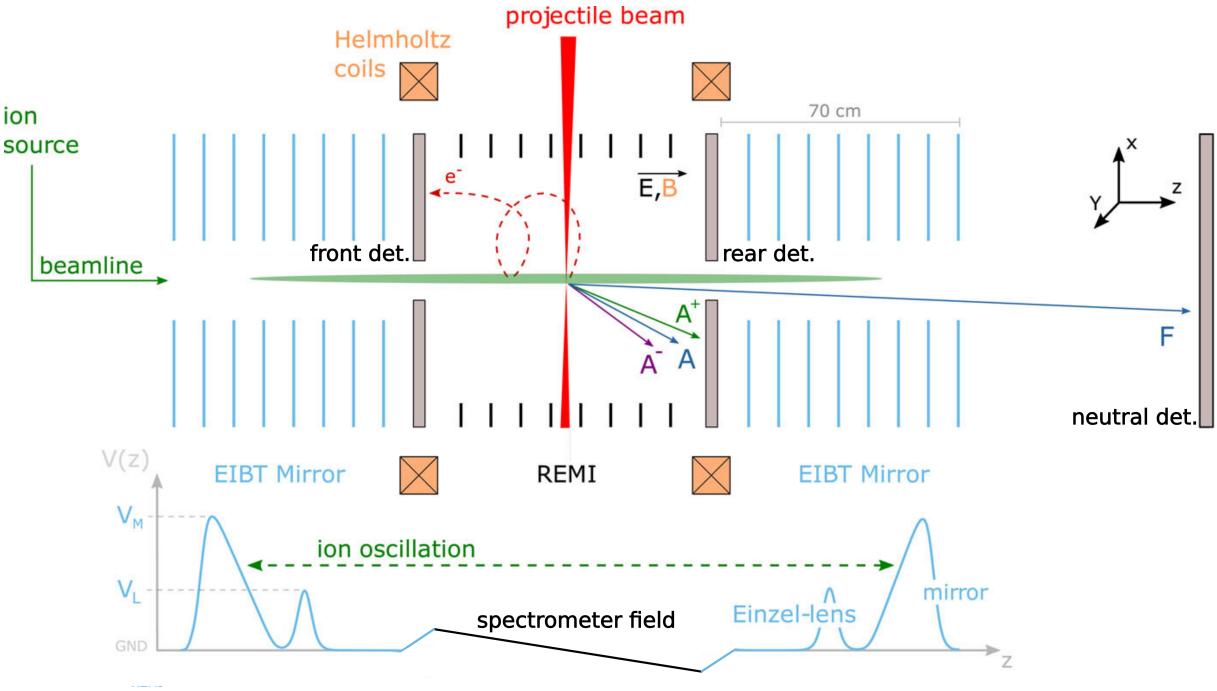

Figure 7: Sketch of the device combination in TrapREMI with an exemplary particle detection scheme and electrostatic potential along the trap axis. Adapted from [27].

Let us consider an ion beam moving in positive z-direction at several keV and fragmenting due to a reaction (see Fig. 7). Its kinetic energy is high compared to typical energies released in the reactions of interest. Thus neutral fragments of the ions created in reactions are prone to have high momentum in the positive z-direction and can be detected on the rear detector in case of higher transversal recoil (A) or pass through the hole in it and be detected by the neutral detector located behind the REMI (F). The detection of the

positive ions (A^+) and the electrons (e^-) is in principle analogous to the usual REMI configuration described in 1.2. The ions, however, require sufficient transversal recoil to be detected. Negative fragments of the ion (A^-) beam can be detected on the rear detector in this scenario (again require sufficient transversal recoil). The detection possibilities described above should only be seen as an example, because different detection schemes can be implemented depending on the reaction of interest.

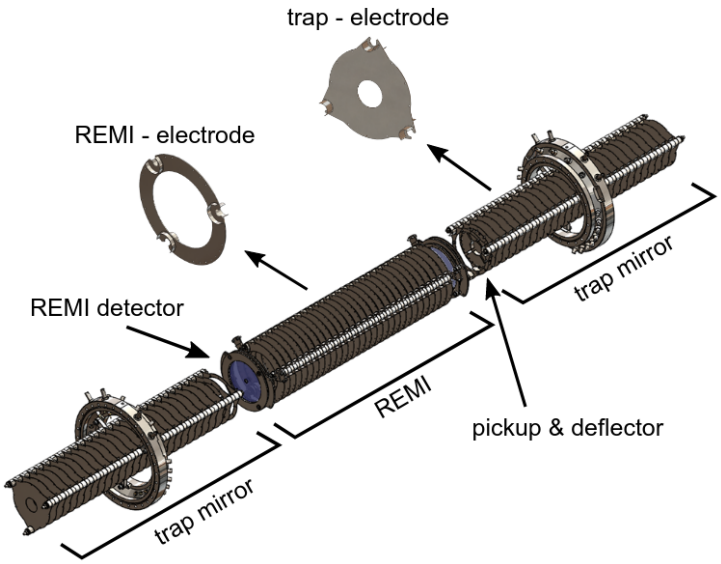

Figure 8: TrapREMI electrode arrangement, source: [26].

Fig. 8 shows the combined electrode arrangement in the TrapREMI. The REMI spectrometer is an array of 30 ring electrodes with a spacing of 20 mm, inner diameter of 120 mm and outer diameter of 172 mm. The magnetic field is created using a Helmholtz coil with radius of 0.7 m and 24 turns.

In order to enable position detection around the hole in the front and the rear detector, a so-called hexanode configuration of delay lines is used (see Fig. 9). Three delay lines are rotated by 60° relative to each other and overlapped. Each has a gap around the hole and consists of a signal and a reference wire. Each pair of two crossed delay-lines is sufficient to reconstruct the position using the same principles as shown in Fig. 6 and previously discussed. Thus only a small star-shaped region covered by maximally one delay line around the hole cannot be used for detection.

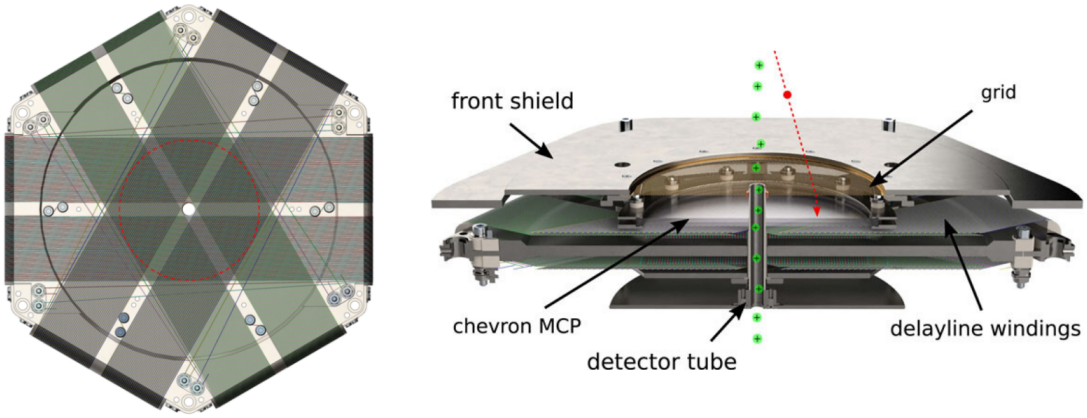

Figure 9: Front and rear REMI detector design. Left: hexanode delay-line configuration (detection area inside the red dashed circle). Right: cross-sectional view. Source: [26].

Detection occurs on the active area of the detector with diameter of 80 mm (marked with dashed red line in Fig.9). In the center it has a dead area with a diameter of 11 mm. In order to reduce the influence on the ion trapping by the detectors, a tube electrode with inner diameter of 5.5 mm goes through the detector holes. Its potential can be adjusted in order to shield the ions from the strong electric field of the MCP. An additional grid electrode is placed in front of the MCP to shield charged particles in the REMI from the electric fields of the MCP and continue the electric field of the REMI up until the detector.

The neutral detector has a simpler design with no hole and a so-called quadanode delay line configuration (two crossed delay lines, as depicted in Fig. 6). It has a round detection area with an 80 mm diameter.

Powering and read-out of the detectors occur through the so-called coupling boxes. Each coupling box is connected to a high voltage power supply and all the different potentials inside a single detector are provided using voltage dividers inside the coupling box. It also couples out the AC part of the MCP back side voltage and the detector wires' voltages (subtracting the reference signal). The resulting signals are amplified and enter the data acquisition system.

1.3 Ion beam generation

Newly installed ion source

During the work on this thesis a new ion source was installed. It is an electron-cyclotron resonance (ECR) based TES-63 ion source by Polygon Physics [33]. Previously an ion source based on impact ionisation by electrons emitted from a filament and accelerated towards an anode was used [26]. Compared to that the new ion source provides a significantly higher ion current and additionally allows the production of negative ions, while remaining compact and relatively simple to operate.

The phenomenon of the ECR is a case of a driven oscillator resonance. An electron in a constant homogeneous magnetic field $\vec{B}$ performs a well-known cyclotron movement (circular motion in the plane orthogonal to the $\vec{B}$) with frequency

$$f_c = \frac{eB}{2\pi m_e} \tag{2}$$

depending only on constants: electron mass m_e, elementary charge e and the magnitude of $\vec{B}$. This oscillation can be driven by an external alternating electric field orthogonal to $\vec{B}$. If the driving field has a frequency equal to the cyclotron frequency, the ECR condition is reached and the electrons are accelerated most efficiently.

We now consider a neutral gas around the electron. The electron will not accelerate endlessly but will collide with a gas particle at some point. Its most probable kinetic energy immediately before the collision is given by the mean free path (corresponding to a certain mean acceleration time) and electric field amplitude. This collision will produce new free electrons with a certain probability. The new free electrons get accelerated before they collide with the next gas particle.

This can be used to create and maintain plasma. A small number of free electrons present in a gas at room temperature can be accelerated causing plasma ignition, a chain reaction increasing the number of free electrons, which then increases the rate of gas ionisation. The plasma then reaches a dynamic equilibrium of production rates. It contains all ions

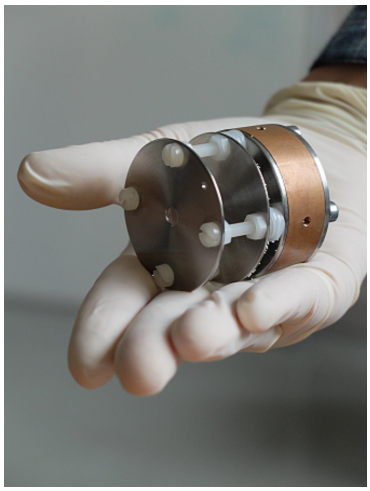

Figure 10: Photo of the ECR cavity, source: [32].

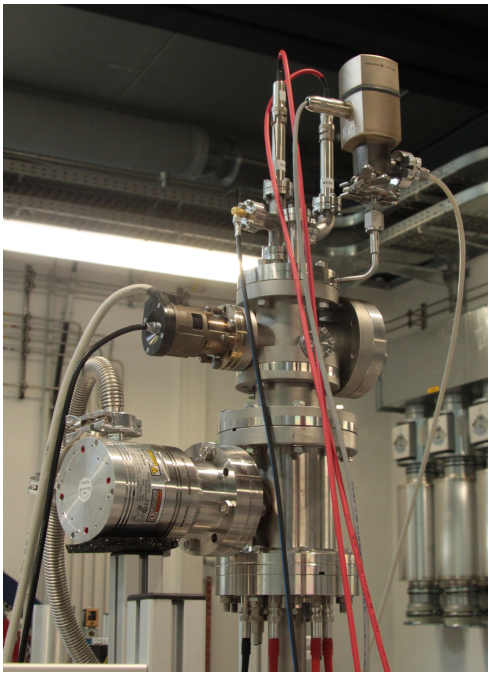

Figure 11: Photo of the ion source chamber.

produced in the collisions (including negative ones), neutral gas particles and free electrons with abundances given by the gas species and the free electron kinetic energy distribution. This distribution depends on the driving power and the gas density.

In the ion source a magnetic field of 82.5 mT corresponding to the electron cyclotron frequency of 2.45 GHz is generated using a permanent magnet and the driving electric field is generated using a miniature cavity (see Fig. 10) connected to a high frequency generator [32]. Gas is introduced into the ion source chamber via an electrically controlled valve. Plasma ignition is achieved using a short pulse of high driving power while no extraction field is present. The plasma is then maintained with a lower driving power. The cavity is biased by a high voltage defining the produced ion kinetic energy at ground potential. The ions are extracted with an electrode at a lower potential with a round opening of 1 mm diameter. By switching the polarity of these voltages, ions of the opposite charge can be extracted. The voltage of the extraction electrode determines the ion-optical properties of the source and thus the form of the outgoing beam. The source produces predominantly singly-charged ions, being able to deliver up to several 10 µA ion beam current.

The source is operated using an electronic control unit as well as a high voltage generation unit and is controlled via a PC using a LabView-based software provided by the manufacturer. The gas flow through the valve, the cavity bias voltage, the extraction voltage and the high-frequency power can be adjusted through the software. One can also program temporal sequences for changing those parameters and stabilize source chamber pressure or measured ion beam current via automatic control of the parameters.

The source is typically operated at some 10^{-5} mbar. To minimize the effect of the gas influx on the EIBT/REMI vacuum, the source was installed with its own vacuum stage, as can be seen in Fig. 11.

Ion beamline

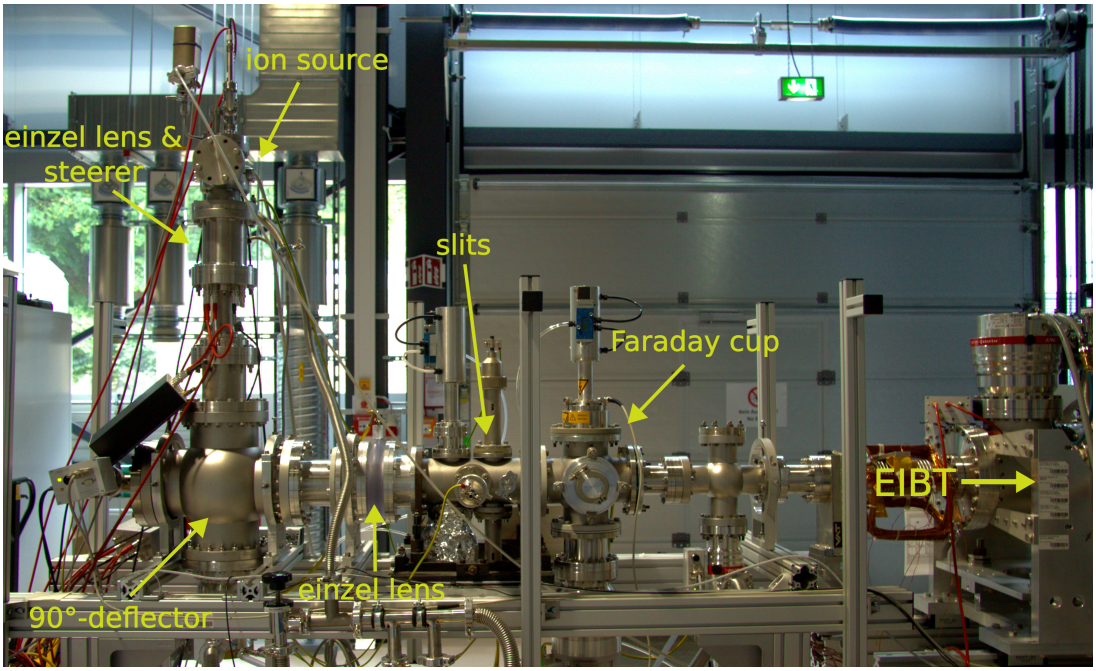

Figure 12: Photo of the ion beamline.

Fig. 12 shows the beamline for ion injection into the EIBT. Ions are produced by the source and accelerated to several keV using an electrostatic field. A stack of electrodes containing an einzel lens and a 4-quadrant-steerer is located directly after the source to focus and align the ion beam.

An electrostatic 90°-deflector is used to bring the ions on the EIBT/REMI axis. Without it a beam of fast neutrals coming from the ion source would enter the REMI and interfere with the experiment. In the ion source a gas for the ion production is injected, providing a target not only for the ion production but also for the neutralisation of already ionised and accelerated particles.

It is followed by an einzel lens allowing further focusing and an arrangement of tunable slits to cut the ion beam mechanically in the transversal direction. Two Faraday cups, one located following the slits and the other behind the EIBT, can be inserted into the ion path to measure the ion beam current.

The beamline contains four differential pumping stages in order to achieve ultra-high vacuum conditions in the EIBT, while remaining connected to the ion source operated at a higher pressure.

1.4 Setup operation

1.4.1 Electrode voltage control

To operate the setup it is necessary to control the voltages of the electrodes. Each EIBT electrode can be individually connected to a power supply but only some of these are connected while the others are kept at ground. REMI spectrometer electrodes are wired in series with equal resistors between them and only the edge electrodes have a feedthrough. The potentials of the grids and the tubes of the REMI detectors can be adjusted individually. Current EIBT and REMI electrode assignment and wiring are shown in Appendix A. An additional einzel lens is implemented before the EIBT entry mirror to enable focusing of the ion beam before entering the EIBT.

The voltage on those electrodes is provided by ISEG NHQ power supplies. For a smoother operation and remote control a simple Python-based application was written during this thesis. It provides a control of the power supplies through byte-wise communication via a RS232 interface using the protocol provided by the manufacturer [21]. The user can simply adjust voltages by entering them inside the electrode scheme and sketch the entered voltages in a plot (see Fig. 13). One can also adjust the voltage ramp speed as well as execute all the further commands provided by the manufacturer via an entry field.

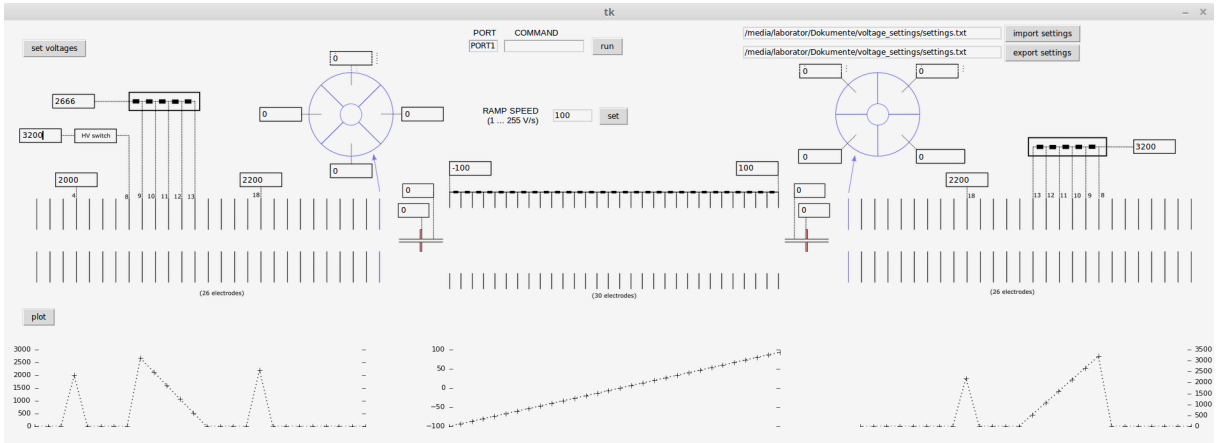

Figure 13: Interface of the power supply control application.

1.4.2 Ion beam storage and monitoring

A typical ion storage procedure starts by first optimizing the ion transport to the first Faraday cup inside the ion beamline using electrodes directly after the source and the 90°-deflector. Then the ion transport to the further Faraday cup behind the trap is optimized using the einzel lenses and the steerers of the EIBT.

In order to store the ions, the mirror potentials are switched on. To allow the ion injection, the entry mirror's outermost electrode is lowered for a certain time interval using a fast high voltage switch. The ion beam can be pulsed via deflection using one of the steerer electrodes directly after the source with another fast switch. Both switches are controlled by a timer module, the timing parameters are inserted via a LabView-based software on a PC. (This timer module also sends trigger signals to the data acquisition system in order to give a reference initial time for each injection cycle.) The EIBT voltages are iteratively adjusted for an optimal storage, using the signal of one of the REMI detectors as a feedback for the ion storage quality as described below.

When an ion beam passes the REMI, some of the ions scatter on the residual gas, landing on the active detector area. The rate of the scattering on the residual gas is proportional to the ion density. Thus the REMI signal provides a very sensitive method for monitoring the ion beam. Single scattered particles can be measured and statistics can be recorded over a large number of injection cycles. One can also display the number of the scattered ions averaged over several cycles on an oscilloscope in real time. This signal however does not provide information on the absolute number of the stored ions because the amount of ions scattered to the detector depends on the beam shape and the exact trajectory. Additionally, at higher density scattering between the stored ions is possible and its rate is not proportional to the density but its value squared.

The ion beam moving towards the neutral detector creates a weak beam of fast neutrals that emerge from the charge exchange with residual gas. Those can be detected on the neutral detector to gain some information about the cross-section of the ion beam. Note that the measured distribution is more complicated than just the averaged cross-sectional

density: it depends on the time the stored ions spend at different positions in the EIBT and the detection probability of the neutralised particles, determined by their kinetic energy.

1.4.3 Data acquisition and primary analysis

MCP and delay line signals from the coupling boxes are amplified using a fast amplifier and directed to a data acquisition system, originally developed for the camera system FlashCam used in Cherenkov telescope array [34]. Our version is set up to digitize and buffer voltage time traces of 4 ns long samples with 12-bit resolution along 24 channels. Data storage can be triggered by a voltage signal on one or several channels of choice. We use one or several MCP channel signals to trigger storage of 256 ns (64 samples) long traces of all channels. Part of this time trace is taken from the buffer before the trigger and the other part is recorded after the trigger. This is necessary due to the fact that some delay line signals may arrive earlier than the corresponding MCP signal. The resulting time traces are stored on a PC. The MCP signals go through a CFD module with a veto feature suppressing the output signal according to an external signal in order to be able to suppress data storage at certain moments in the ion injection/storage cycle.

The data is then loaded to a custom analysis software based on Go4 (GSI Object Oriented On-line Off-line system) framework [28], written in C++ and utilising ROOT. Using a digital peak finding algorithm (constant fraction discriminator) time traces are converted to counts at certain times for each channel. Then combinations of single counts on seven (for hexanode delay lines) or five (for quadanode delay lines) channels corresponding to a single detector are selected if they fulfill the following condition: The counts stem from the same trigger event and the sum of the measured times on two ends of a single delay-line relative to the MCP count lie in a narrow range. It is fulfilled for genuine detector hits because the time in which a signal traverses the whole length of the wire is constant. From these counts detector hits with corresponding time and position are reconstructed. The time of the hit is determined by the MCP count and the position is calculated from the delay line signal times.

2 Supersonic gas jet as a cold target

In order to provide the TrapREMI setup with a cold atomic/molecular target for the crossed-beam experiments, a supersonic gas jet has been assembled in this work. In such an apparatus gas expands from a reservoir at high pressure (several bars) into a low-pressure vacuum chamber through a miniature nozzle (⌀30 µm nozzle used in this work). During the expansion the thermal energy is transformed into directed kinetic energy of the particles, while the velocity spread in the gas is significantly reduced. Hence a cold gas beam moving at supersonic speed is created.

This chapter describes some basic theoretical background for the jet generation (Section 2.1) as well as the design of the assembled setup (Section 2.2). A design of the jet setup by C. D. Schröter was used to upgrade the TrapREMI. This design is commonly utilised in our group. Thus no concrete calculations were needed and the design process is not described in this work, only the general considerations. Additionally, some estimations are given that may be useful for experiments with the jet target.

2.1 Theoretical basics

This section is meant to introduce the basic dynamics of a steady (i.e. time-independent) compressible flow inside a nozzle (1D-model) and qualitative properties of the flow from a nozzle into a vacuum chamber. The latter is more complex and typically involves numerical simulations for a given geometry (2D-model in case of cylindrical symmetry). Both are based on calculations and qualitative discussions in [16] and [29].

One-dimensional nozzle flow

Flow through a nozzle with a varying cross-sectional area A, exhibiting cylindrical symmetry, can be well approximated by assuming that the flow is steady (time-independent) and one-dimensional (flow velocity perpendicular to the symmetry axis is zero), as long as

the rate of change of the cross-sectional area is small [16]. We denote the position along the nozzle axis by x. Fig. 14 depicts such a nozzle. According to the assumptions made, the properties of the flow, namely the flow velocity w (i.e. the average velocity of gas particles at a certain position), density ρ, pressure P and temperature T are constant in time and over the cross-section, they only depend on the position x. We also assume the continuous ideal gas approximation.

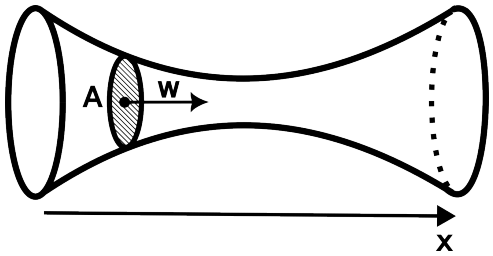

Figure 14: Drawing of an exemplary nozzle with varying cross-section.

The relation between the cross-sectional area A and the flow velocity w can be derived from common thermodynamics relations [16]:

$$\frac{1}{A}\frac{\mathrm{d}A}{\mathrm{d}x} + \frac{1}{w}\frac{\mathrm{d}w}{\mathrm{d}x}\left(1 - \frac{w^2}{c^2}\right) = \frac{1}{A}\frac{\mathrm{d}A}{\mathrm{d}x} + \frac{1}{w}\frac{\mathrm{d}w}{\mathrm{d}x}(1 - M^2) = 0 \ , \tag{3}$$

introducing the Mach number M as the ratio of the flow velocity to the speed of sound c.

For subsonic flow ($M < 1$): w increases with decreasing A: $\frac{\mathrm{d}A}{\mathrm{d}x} < 0 \Rightarrow \frac{\mathrm{d}w}{\mathrm{d}x} > 0$ and vice versa $\frac{\mathrm{d}A}{\mathrm{d}x} > 0 \Rightarrow \frac{\mathrm{d}w}{\mathrm{d}x} < 0$. For the supersonic flow ($M > 1$) the situation is reversed: $\frac{\mathrm{d}A}{\mathrm{d}x} > 0 \Rightarrow \frac{\mathrm{d}w}{\mathrm{d}x} > 0$ and $\frac{\mathrm{d}A}{\mathrm{d}x} < 0 \Rightarrow \frac{\mathrm{d}w}{\mathrm{d}x} < 0$. If the sonic flow ($M = 1$) is to be achieved, $\frac{\mathrm{d}A}{\mathrm{d}x} = 0$ follows, meaning it can only occur at a local minimum of A, the so-called nozzle throat. It is of course only achievable if the pressure difference between the ends of the nozzle is sufficiently high.

Therefore one simple choice for the creation of supersonic flow would be a nozzle first converging to accelerate the subsonic flow, reaching the speed of sound at the throat and then diverging for further acceleration of the supersonic flow.

The flow velocity at some position in the nozzle with temperature T and pressure P can be calculated from energy conservation by assuming an adiabatic expansion of a gas

with adiabatic constant κ and molar mass m_{mol} from a reservoir with pressure P_0 and temperature T_0 [16].

$$w = \sqrt{2\frac{\kappa}{\kappa-1}\frac{RT_0}{m_{\mathrm{mol}}}\left(1-\frac{T}{T_0}\right)} = \sqrt{2\frac{\kappa}{\kappa-1}\frac{RT_0}{m_{\mathrm{mol}}}\left[1-\left(\frac{P}{P_0}\right)^{(\kappa-1)/\kappa}\right]} \ . \tag{4}$$

From this the maximal achievable flow velocity w_{max}, corresponding to the expansion into absolute vacuum ($P = 0$), is given by [16]

$$w_{\mathrm{max}} = \sqrt{2\frac{\kappa}{\kappa-1}\frac{RT_0}{m_{\mathrm{mol}}}} \ . \tag{5}$$

This relation for the maximal flow velocity also holds for the free jet expansion (described in the following discussion) [29]. In a properly functioning jet setup significant cooling takes place, and the mean velocity almost reaches w_{max}.

Achieving sonic flow ($w = c$) at the nozzle throat according to eq. (4) corresponds to the pressure ratio between the nozzle throat ($P = P^*$) and the initial reservoir [16]

$$\frac{P^*}{P_0} = \left(\frac{2}{\kappa+1}\right)^{\kappa/(\kappa-1)} \ . \tag{6}$$

This relation specifies the condition for the ambient pressure around the nozzle exit P_a to achieve a supersonic flow in a convergent-divergent nozzle [16]. The term depending only on κ can be further estimated from above with a numerical value for all known gases [29].

$$P_a \leq \left(\frac{2}{\kappa+1}\right)^{\kappa/(\kappa-1)} \cdot P_0 \leq \frac{1}{2.1} \cdot P_0 \ . \tag{7}$$

For further discussion it is important to mention, that a convergent nozzle creates a flow accelerating along the nozzle, reaching the speed of sound at its exit and an orifice with constant cross-sectional area creates a homogeneous sonic flow, as long as the critical pressure ratio condition, eq. (7), is fulfilled.

Free jet expansion

For small dimensions of the nozzle throat typically used for molecular/atomic beam creation (usually of order 5 µm - 100 µm) it is significantly easier to produce convergent

nozzles or orifices of constant cross-sectional area. A reservoir at high pressure (typically several bars) is connected to a vacuum chamber through such a nozzle, fulfilling the critical pressure ratio condition, eq. (7). At the exit of the nozzle sonic speed is reached and the pressure is given by eq. (6).

If the pressure at the nozzle exit is higher than the ambient pressure in the vacuum chamber the gas expands further into the chamber reaching supersonic speeds. It qualitatively corresponds to an increase of the cross sectional area in the 1D-model. Assuming rotational symmetry along the nozzle axis, further expansion can be adequately described by a two-dimensional model.

In the frame of reference moving with the flow velocity w a pressure disturbance propagates with the speed of sound c. In the laboratory frame this disturbance moves with the velocity $c - w$ in the upstream direction and the velocity $c + w$ in the downstream direction. Thus in the supersonic region there is no propagation in the upstream direction, meaning that the supersonic flow does not "sense" the downstream boundary conditions. Due to that the free jet can expand to pressures below the ambient pressure and the so-called shocks provide the only mechanism to adjust the flow to the boundary conditions downstream. The shocks are small regions of unsteady flow with high pressure gradient, where the flow rapidly transitions from supersonic to subsonic [16]. Understanding the exact dynamics inside those is not necessary to operate a cold gas jet, however it is of practical value to know their shape and approximate positions.

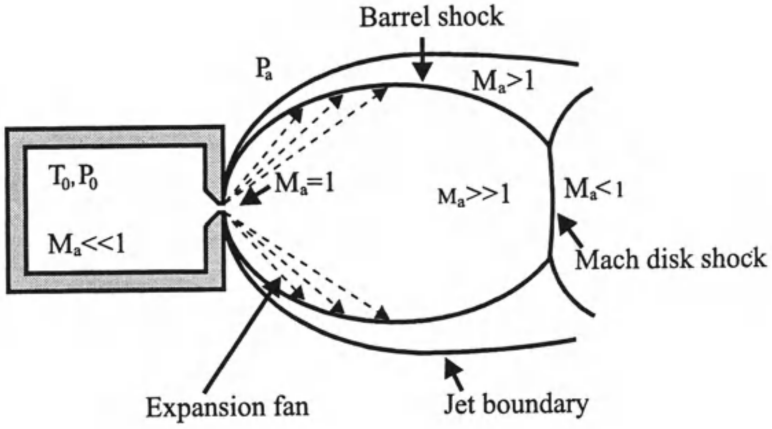

Figure 15: Typical free jet structure, source: [16].

A typical shock structure and flow velocity distribution in a free jet is shown in Fig. 15. Around the nozzle exit there is a region of supersonic expansion ($M \gg 1$), also called zone of silence, which is surrounded by the barrel shock on the side and the Mach disk shock in the direction of the expansion [16].

The distance between the nozzle exit and the Mach disk x_M can be usually estimated by the following empirical formula [16]

$$x_M = 0.67 d \sqrt{\frac{P_0}{P_a}} \ , \tag{8}$$

where d is the diameter of the nozzle exit, P_0 the pressure upstream of the nozzle and P_a the ambient pressure in the expansion chamber.

It is important to mention that at lower pressures the mean free path increases, making the continuous gas model, assumed in this discussion, less accurate.

Skimmed jet

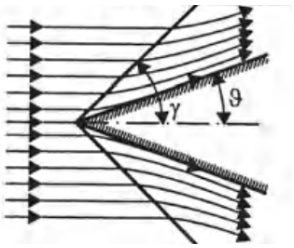

Figure 16: Streamlines for supersonic flow over a sharp cone. Solid lines depict the arising shocks, source: [16]

In order to conduct experiments with a cold gas target one needs to guide the gas from the region of supersonic expansion into the region, where reactions take place. A sharp conical skimmer with a small opening at its tip is used to cut through the Mach disk and extract the gas from the region of the supersonic flow. Due to the boundary conditions imposed by the skimmer walls, additional shocks arise from its opening's edges, connecting to the shock structure of the jet expansion (shocks caused by a sharp cone in a supersonic flow illustrated in Fig. 16) [16]. The opening is not affected by the shocks and the gas can move to the next vacuum stage at a lower ambient pressure without disturbance.

A second skimmer or an orifice is typically used to further narrow down the diameter and the velocity distribution perpendicular to the jet expansion direction. The beam then optionally traverses one or several pumping stages to reduce the ambient pressure to a value intended for the experiment.

Afterwards, the beam enters the reaction region and finally is collected behind it in the so-called dump stage using a turbo-molecular pump directed at the gas jet. Dump might also have several pumping stages in order to avoid a pressure increase in the reaction region due to back-scattering jet particles.

Usually, for the major part of the jet's length the density is low enough to assume free molecular flow. The density of the jet ρ at a certain distance r from the nozzle scales reversely proportionally to the surface area of a corresponding sphere around the beam source with a radius r.

$$\rho \propto \frac{1}{r^2} \tag{9}$$

2.2 Design and assembly

This section discusses some basic considerations that need to be taken into account when designing a jet setup (2.2.1), then describes the implemented design (2.2.2 and 2.2.3) and the assembly process (2.2.4).

2.2.1 General technical considerations

The nozzle size is an important parameter. The larger it is, the larger the size of the supersonic flow region, meaning a simpler extraction and a higher target number for the reaction. On the other hand, it increases the mass flow deflected by the first skimmer, which then fills the first chamber. This leads to a higher pressure in the first chamber or requires more powerful pumps to compensate for.

In order to preserve as high target density as possible it is important to keep the distance between the jet source and the experiment as short as possible. High target gas density is beneficial for higher reaction rates as well as higher signal-to-background ratio. Simultaneously, one needs to guarantee that the gas inlet for the jet generation does not affect the pressure in the chamber, where reactions take place. Thus depending on the requirements for the ambient pressure at the experiment site and for the jet density one should decide an optimal trade-off between those. It is also beneficial to keep the pumping stages as short along the jet axis as possible.

The size and the structure of the supersonic flow region depend on different parameters that may vary throughout the different experiments with the same setup (e.g. reservoir pressure, nozzle geometry, gas species) and is typically rather small. Thus it is important to provide a possibility to fine-tune the relative position between the nozzle and the first skimmer, while operating the jet.

2.2.2 Nozzle and skimmers arrangement

The first two jet stages are mounted one inside the other, as can be seen in Fig. 17. The chambers are only connected via a conical skimmer with a ⌀200 µm opening. A second conical skimmer with a ⌀400 µm opening is placed coaxially behind the first one at the exit of the outer chamber. The geometry of the chambers is such, that the combined arrangement has two connections for either chamber on the sides not used for the gas inlet or the jet extraction. On those connections a turbo-pump and a pressure gauge for either chamber is mounted.

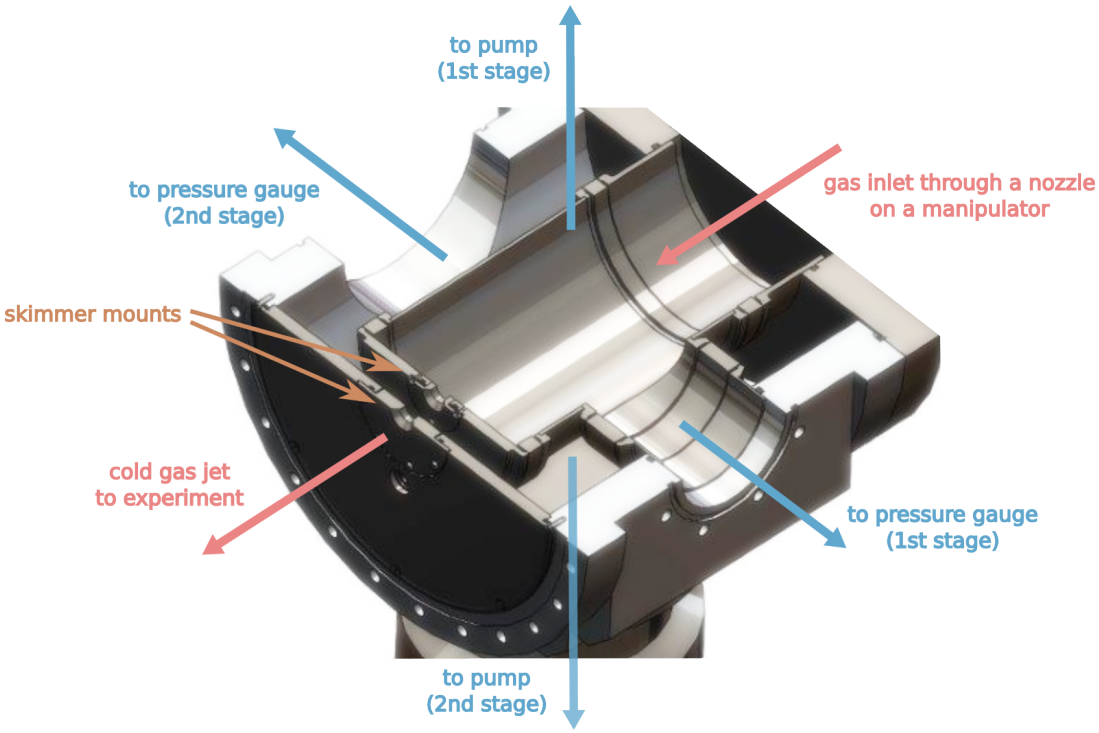

Figure 17: CAD drawing of the first two chambers for cold gas jet generation.

High pressure gas (several bars) is connected to a stainless steel tube with a ⌀30 µm nozzle mounted on its end, the gas can only exit through the nozzle. The tube is inserted into the inner vacuum chamber where the jet expansion happens. The tube is welded on a flange with a gas feedthrough and mounted on a manipulator (see Fig. 18) enabling the tuning of the nozzle position relative to the fixed first skimmer. It is realized by tilting and translating the mounting flange using an arrangement of precision screws.

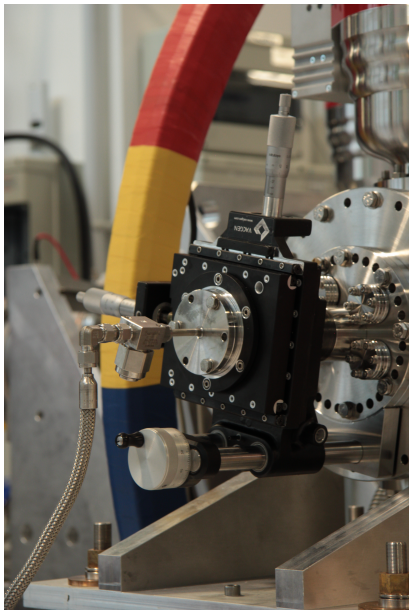

Figure 18: Gas feedthrough on a manipulator.

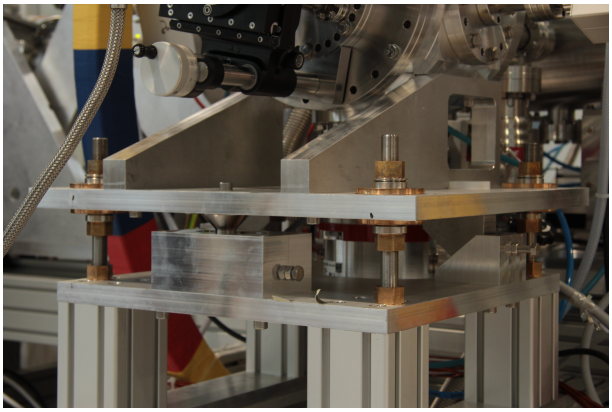

Figure 19: Jet alignment table.

The whole arrangement is installed on an alignment table (see Fig. 19). Using the screws, located at each corner of the table, one can adjust the height and tilt the table by changing the heights of the corners. The arrangement can also be rotated in the plane of the table by utilizing additional screws and rotating mounts. Those features are crucial to align the jet axis given by the two first skimmers with the downstream stages.

2.2.3 Full jet setup

We decided to build a 3-stage jet setup where the first two stages are required to skim and collimate the expanding gas using a pair of conical skimmers (as described in 2.2.2) and the third stage further reduces the ambient pressure before the REMI (see Fig. 20). After the REMI the beam enters a two-stage dump.

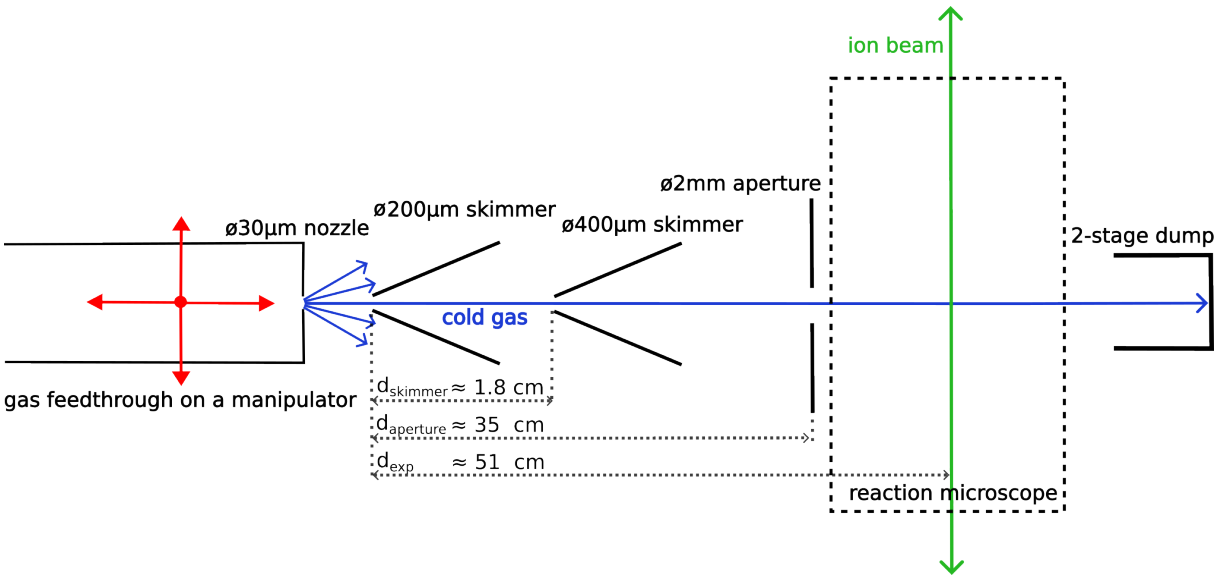

Figure 20: Sketch of the jet setup.

From the sizes of the apertures and the distances we can estimate the transversal size of the jet. The smallest opening angle on the path of the jet after the first skimmer is given by the 2 mm aperture before the REMI. We can assume that the velocities do not change after the first skimmer (free molecular flow). The opening angle of the jet is less or equal to the angle between the line connecting the upper edge of the first skimmer opening with the upper edge of the aperture and the corresponding line connecting the lower edges. The jet diameter at the reaction site can be then estimated from simple geometrical considerations:

$$\varnothing(\text{jet}) \leq \frac{d_{\text{exp.}}}{d_{\text{aperture}}} \left(\varnothing(\text{aperture}) - \varnothing(\text{1st skimmer})\right) + \varnothing(\text{1st skimmer}) \approx 2.8\,\text{mm} \qquad (10)$$

This corresponds to the maximal ratio between the transversal ($v_{\text{jet},\perp}$) and the longitudinal jet velocity (v_{jet}) of:

$$\left(\frac{v_{\text{jet},\perp}}{v_{\text{jet}}}\right) \leq \frac{\varnothing(\text{jet})}{d_{\text{exp.}}} \approx 5 \cdot 10^{-3} \qquad (11)$$

One can see photos of the assembled jet setup in Fig. 21 and 22.

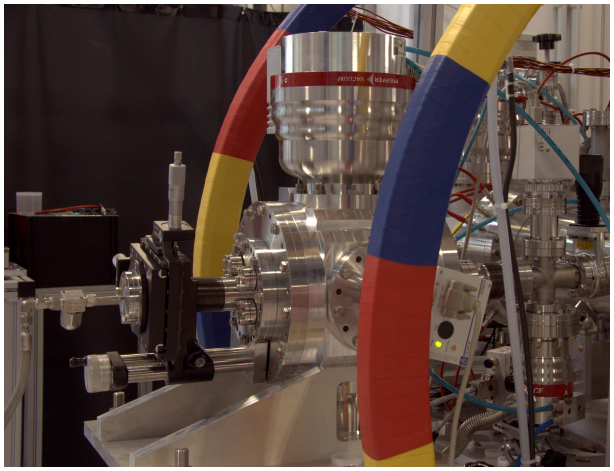

Figure 21: Jet generation setup photo.

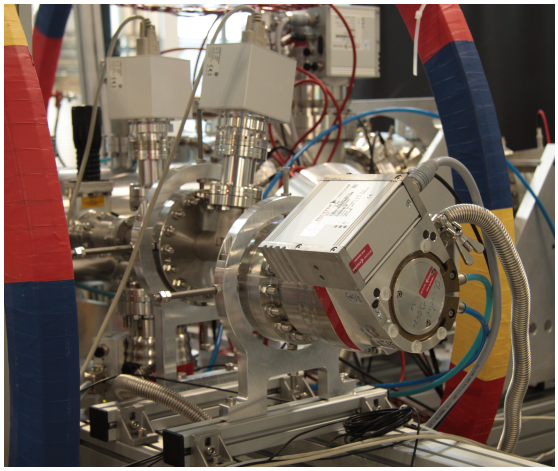

Figure 22: Jet dump photo.

2.2.4 Assembly process

First, the arrangement for the jet generation described in Section 2.2.2 was assembled. The inner chamber was inserted into the outer one and the connections were dynamically sealed using polymer o-rings. As a further step the first skimmer was mounted on the exit of the inner chamber. The mounting plate for the second skimmer was then attached to the exit side of the outer chamber and the skimmer was mounted on it. The mount of the second skimmer allows a slight variation of the skimmer position by hand for alignment purposes. The turbo-pump for the second stage was mounted on the lower connection of the chamber. Then the whole arrangement was mounted on the alignment table and the turbo-pump for the first chamber was mounted on top, followed by the pressure gauges on the sides. It was then placed in its position near REMI on an ITEM table.

Next, the two dump stages were installed behind the REMI chamber omitting the final pump in order to have visual access to the whole gas pathway. All flanges as well as the two skimmers were aligned on the axis given by the entrance and the exit windows of the REMI using a telescope. Finally, the third jet stage was installed, connecting the first two stages to the REMI and the dump pump was installed at the end of the jet.

In a well-aligned working jet, the mass flow reaching the final dump stage takes its maximal value. The pressure in a vacuum chamber is indicative of the mass flow entering it. In order to finalize the initial alignment, all the pumps were turned on and the gas inlet to the nozzle opened. The pressure in the dump stage was maximised by subsequent optimization of the pressure in consecutive stages. It was done through adjusting the relative position between the nozzle and the first skimmer (using the manipulator) as well as the orientation of the nozzle arrangement (using the alignment table).

3 Ion-atom collision experiment: electron capture by an Ar^+ ion from an Ar atom

In order to test the feasibility and limitations of the ion-atom collisions experiments in the TrapREMI, we observed charge exchange (CX): a singly-charged ion captures an electron from a neutral atom. It was decided to observe symmetric CX, i.e. between the same species, such that most reactions occur resonantly, meaning a high cross-section. Argon was used because it could be easily accessed in the lab, is widely explored experimentally and as an atomic gas it has a significantly simpler excitation spectrum compared to molecules. The absolute cross-section for the process involving argon atoms at collision energy of 2 keV is $(2.405 \pm 0.061) \cdot 10^{-15}\,\mathrm{cm}^2$ [10].

Several experiments were performed with other target (He, O_2, N_2) in less detail to check the validity of the signal and its dependence on the mass of the particles involved. Those provide no new insight in the context of this work and thus only the argon-argon experiments will be discussed here.

3.1 Preparations

3.1.1 Alignment

The reaction is induced by crossing the ion beam with the atomic gas jet. One can manipulate both beams to achieve a good overlap between them.

For initial mutual alignment of the two beams, a continuous ion beam directly from the ion source (not stored in the EIBT) was used because it has a higher ion density and the beam can be easily guided: The direct ion beam can be steered and focused using the electrodes of the EIBT and it can be monitored on the neutral detector behind the EIBT. In contrast, it is not easy to shift or tilt a stored beam in an understandable manner as the storage itself requires certain potentials.

Initial alignment was performed in the following way: The guiding of the ion beam was varied until the overlap with the target was good enough to observe some characteristic signature of the reaction (described in the section 3.3). Then this signal was maximized via finer variation of the EIBT voltages. Afterwards the signal was further optimized by adjusting the jet direction using its alignment table. It was followed by subsequent optimization via ion beam fine-tuning.

First, measurements were done using a direct ion beam, later the same experiment was conducted with stored ions. After some oscillations in the trap, the limitations due to the detector holes impose rather strict conditions for the transversal position and velocity distribution in the interaction region. After the ion storage was achieved, the beam overlap was immediately good and did not require additional alignment (this would probably not be the case without jet optimization in the initial alignment).

3.1.2 Detection scheme

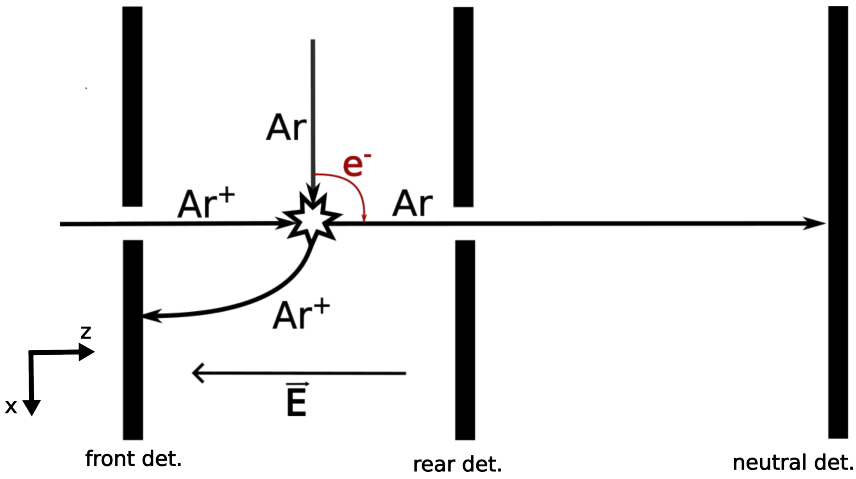

Figure 23: Argon symmetric charge exchange detection scheme.

The following detection scheme was chosen for the argon symmetric CX experiment (see Fig. 23): When a reaction occurs, the projectile gets neutralized and passes through the hole of the rear detector before it hits the neutral detector. The ion beam is deflected away from the neutral detector using an EIBT steerer-electrode in direct beam measurements, in case of trapping the stored ions are reflected by the mirror potential. The ionized target atom is extracted onto the front detector with a homogeneous electric field. The two products of a single charge exchange event have strong correlation in their time-of-flight (ToF) - time duration between the collision and their arrivals on the detectors.

We do not possess information about the exact moment when a single reaction takes place and can only measure the arrival times of the products relative to some arbitrary zero time. Nevertheless, for the two products of the same event the difference of those measured arrival times is equal to the ToF difference, because the reaction time cancels out. We can thus identify coincident particles in the arrival time difference spectrum ("time spectrum" in further discussion): a histogram of time differences between all the possible pairs of hits at the two involved detectors. All the pairs of the products of the same reaction will form a narrow peak (or several) while the uncorrelated pairs will be randomly distributed. One can select the correct pairs via a time window condition on such peak(s). Although, some random pairs will accidentally match it and be still present as a background.

3.2 Kinematics

In this section we discuss the kinematics of the reaction products and the reconstruction of certain reaction properties. All kinematic properties are given in the lab frame. We assume an initial ion projectile of mass m_p and charge q (in the experiment equal to the elementary charge) moving in positive z-direction with a kinetic energy E_0 (fixed by the ion source voltage and thus equal for all masses present in the ion beam). The neutral target particle of mass m_t has velocity v_{jet} along the x-axis (the mean velocity is equal for all masses present in the jet). According to momentum conservation the momentum sum of the target and the projectile does not change. We name the momentum change for the target particle $\Delta\vec{p} = (\Delta p_x, \Delta p_y, \Delta p_z)$, the corresponding change for the projectile is then $-\Delta\vec{p}$. The individual masses change by one electron mass m_e. We denote the distance from the reaction site to the front detector by d_f and to the neutral detector by d_n.

3.2.1 Time-of-flight / longitudinal momenta

The ionized target atom (recoil ion) experiences a momentum change Δp_z along the z-axis and is accelerated by a homogeneous electric field of strength $\mathcal{E}$ towards the detector. Its ToF is then given by

$$t_t = \sqrt{\frac{2(m_t - m_e)d_f}{q\mathcal{E}} + \frac{1}{(q\mathcal{E})^2}\Delta p_z^2} - \frac{\Delta p_z}{q\mathcal{E}} \quad . \tag{12}$$

The projectile velocity after the reaction is $\sqrt{\frac{2E_0}{m_p}} - \frac{\Delta p_z}{m_p + m_e}$, it is neutral and thus does not experience any acceleration in the spectrometer field. Its ToF to the neutral detector is

$$t_p = \frac{d_n}{\sqrt{\frac{2E_0}{m_p}} - \frac{\Delta p_z}{m_p + m_e}} \quad . \tag{13}$$

The experimentally measured difference between those is then

$$t_{\text{diff.}} = t_t - t_p = \sqrt{\frac{2(m_t - m_e)d_f}{q\mathcal{E}} + \frac{1}{(q\mathcal{E})^2}\Delta p_z^2} - \frac{\Delta p_z}{q\mathcal{E}} - \frac{d_n}{\sqrt{\frac{2E_0}{m_p}} - \frac{\Delta p_z}{m_p + m_e}} \quad . \tag{14}$$

We can simplify the above equation by making the following approximations: The electron mass is significantly smaller than the projectile and target masses relevant for this

work, and thus can be ignored ($\frac{m_e}{m_t}, \frac{m_e}{m_p} \leq \frac{m_e}{m(^{36}\mathrm{Ar})} = 1.5 \cdot 10^{-5}$). We further assume that the momentum gain in the reaction is much smaller than the momentum gain from acceleration in the spectrometer field: $\Delta p_z \ll \sqrt{2 m_t d_f q \mathcal{E}}$ and much smaller than the initial projectile velocity times the target mass: $\Delta p_z \ll m_t \sqrt{\frac{2E_0}{m_p}}$. We can then linearize t_t in $\frac{\Delta p_z}{\sqrt{2 m_t d_f q \mathcal{E}}}$ around zero and linearize t_p in $\frac{\Delta p_z}{m_t \sqrt{\frac{2E_0}{m_p}}}$ around zero, obtaining

$$t_{\text{diff.}} = \sqrt{\frac{2 d_f m_t}{q\mathcal{E}}} - \frac{d_n \sqrt{m_p}}{\sqrt{2E_0}} - \left(\frac{1}{q\mathcal{E}} - \frac{d_n m_p}{2E_0 m_t} \right) \Delta p_z + \mathcal{O}(\Delta p_z^2) \ . \tag{15}$$

The above expression can be used to reconstruct Δp_z in such experiments. In case the target contains particles with several different masses, the larger mass corresponds to a longer ToF and thus larger $t_{\text{diff.}}$ value. For the projectile a greater mass means a lower velocity and thus longer ToF, which corresponds to a smaller $t_{\text{diff.}}$ value.

An interesting parameter to observe in such reactions is the Q-value - the difference between the total internal energy before and after the reaction. It gives insight into the internal states involved in the reaction. From energy conservation follows

$$\begin{aligned} E_0 + \frac{m_t v_{\text{jet}}^2}{2} = & \frac{(\sqrt{2 m_p E_0} - \Delta p_z)^2 + \Delta p_x^2 + \Delta p_y^2}{2(m_p + m_e)} \\ & + \frac{\Delta p_z^2 + (m_t v_{\text{jet}} + \Delta p_x)^2 + \Delta p_y^2}{2(m_t - m_e)} + Q \ . \end{aligned} \tag{16}$$

Next we assume that the momentum changes due to the reaction and the momentum of the neutral particle in the jet are both significantly smaller than the total momentum of the incoming projectile (ions have kinetic energy of several keV). Ignoring contributions of higher order in Δp_x, Δp_y, Δp_z, v_{jet} and their combinations together with simplifying the above equation leaves us with

$$Q = \frac{\sqrt{2 m_p E_0}}{m_p + m_e} \Delta p_z + \frac{m_e}{m_p + m_e} E_0 + \mathcal{O}(\Delta p_x^2, \Delta p_y^2, \Delta p_z^2, v_{\text{jet}}^2, \Delta p_x v_{\text{jet}}) \ . \tag{17}$$

Here the electron mass can be neglected in the first additive term.

Next we would like to express Q through the measured $t_{\text{diff.}}$ and some constants that can be calibrated using reference data for certain experimental conditions. We introduce t_0

as some arbitrary reference value of $t_{\text{diff.}}$. Using eq. (15) we can rewrite eq. (17) in the following form

$$\begin{aligned} Q(t_{\text{diff.}}) &= Q(t_0) + \frac{\mathrm{d}Q}{\mathrm{d}t_{\text{diff.}}} \cdot (t_{\text{diff.}} - t_0) \\ \text{with } \frac{\mathrm{d}Q}{\mathrm{d}t_{\text{diff.}}} &= -\sqrt{\frac{2E_0}{m_p}} \left(\frac{1}{q\mathcal{E}} - \frac{m_p}{m_t} \cdot \frac{d_n}{2E_0} \right)^{-1} \quad . \end{aligned} \tag{18}$$

The values $Q(t_0)$ and $\frac{\mathrm{d}Q}{\mathrm{d}t_{\text{diff.}}}$ can be calibrated from the mean time values of at least two time spectrum peaks with well-known Q-values.

The resolution can be directly observed from the widths of the peaks. It depends on two experimental parameters: the uncertainty in the distance to the detector due to the size of the reaction region as well as the stability and homogeneity of the electric field along the trajectory of the recoil ions. The latter has negligible effects compared to the width of the gas jet. Its influence on the resolution can be estimated from

$$\left| \frac{\mathrm{d}Q}{\mathrm{d}d_f} \right| = \sqrt{\frac{m_t E_0}{m_p q \mathcal{E}}} \left(\frac{1}{q\mathcal{E}} - \frac{m_p}{m_t} \cdot \frac{d_n}{2E_0} \right)^{-1} \cdot \frac{1}{\sqrt{d_f}} \quad . \tag{19}$$

This limits the energy resolution for a supersonic jet of a few millimeters width. There is a possibility of so-called time-focusing for significantly reducing this effect. This is shortly discussed in Section 3.4.2.

3.2.2 Position / transversal momenta

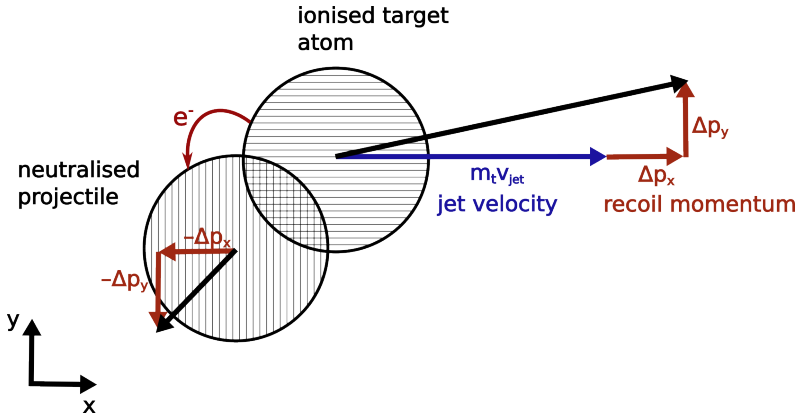

Figure 24: Transversal momenta of the products directly after a CX reaction.
(Recoil momentum may also have a component along the z-axis not depicted here.)

Let us consider a CX reaction taking place at the position (x_0, y_0). Fig. 24 illustrates the transversal momenta immediately after it. The spectrometer field does not accelerate the recoil ion in the xy-plane and its final position on the front detector is given by (ignoring mass change from ionization)

$$\begin{bmatrix} x_t \\ y_t \end{bmatrix} = \begin{bmatrix} x_0 + (v_{\text{jet}} + \frac{\Delta p_x}{m_t})t_t \\ y_0 + \frac{\Delta p_y}{m_t} t_t \end{bmatrix} \quad . \tag{20}$$

The final position in case of $\Delta\vec{p} = 0$: $(x_0 + v_{\text{jet}} t_t,\ y_0)$ can be identified as the centre-of-mass of the measured detector hit position distribution as long as the reaction conditions fulfill cylindrical symmetry around the z-axis (practically fulfilled in this experiment: $v_{\text{jet}} \ll \sqrt{\frac{2E_0}{m_p}}$). Then the transversal recoil momenta can be reconstructed in a straightforward manner from the final positions on the detector. It is important to note that for an acceptable momentum resolution the size of the final distribution needs to be larger than the size of the reaction region (i.e. uncertainty in (x_0, y_0)). The initial target momentum distribution may further widen the measured momentum distribution.

For the projectile the situation is identical, with the only difference that it does not have directed initial velocity along the x-axis. It is less sensitive to $\Delta\vec{p}$ because its ToF is typically shorter. Additionally, the initial transversal momentum distribution is given by the source emittance combined with ion guiding/storage, meaning a more complicated position-dependent distribution.

Overall, the recoil ions' positions can be used to characterize the transversal recoil momentum, while the hit position of the projectile can be used to monitor the ion beam reaching the jet. The transversal momentum resolution is typically lower than the longitudinal one.

3.3 Results

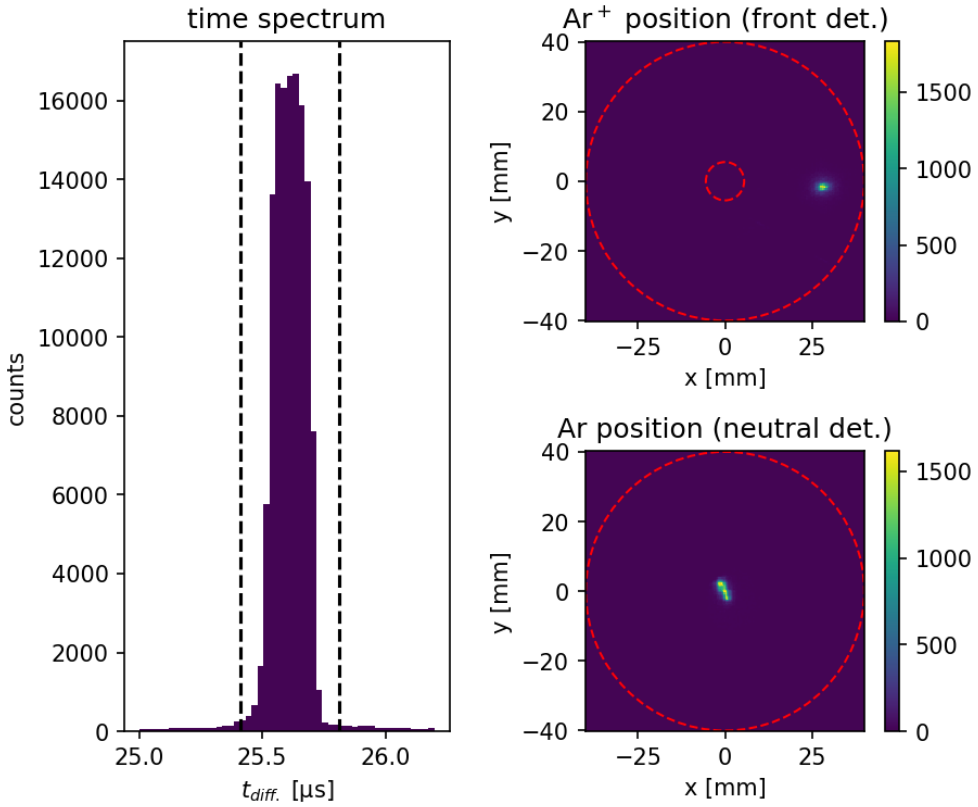

Figure 25: Observed reaction signature. Left: strong peak in the time spectrum. Right: positions of the detector hits from the strongest time peak (condition indicated with black lines in the left plot), red circles indicate the effective detector areas.

The reactions were conducted at 2 keV collision energy. The signature of the reaction is a strong peak in the time spectrum, corresponding to the resonant CX between the ground state ^{40}Ar neutral atom and the ground state $^{40}Ar^+$ singly charged ion (see Fig. 25). The detected positions corresponding to this time peak form a spot on the front detector shifted along the jet axis and a spot near the center of the neutral detector.

3.3.1 Direct vs. stored ion beam

The experiments were conducted first using a direct continuous ion beam (without storage) that was transversally cut by the slits in the beamline and focused approximately onto the rear detector position (to ensure best passage through the detector hole). The best

measured signal-to-background ratio for the main peak was ca 430:1. Later the same measurement was performed with a 10 µs ion bunch stored in the EIBT. The reactions were recorded for storage times between 3 ms and 100 ms. In this case the signal-to-background ratio was ca 900:1. This improvement can be attributed to the different nature of the background events for the two cases. Sources of background in common are dark counts of the MCP and collisions with the residual gas.

Apart from that, a continuous ion beam brings along a fast neutral beam, consisting of former ions that have captured an electron in the beamline, where residual gas pressure is some orders of magnitude higher than in the REMI chamber. Those can be detected on the neutral detector and form the majority of hits on it. While those do not correlate in time with the hits on the front detector, this increases the number of detector hit pairs accidentally matching the coincidence condition. The majority of the background hits on the front detector can be attributed to particles emerging from the collision of the ion beam with the tube or other surfaces of the rear detector. Those can be reduced by properly preparing the ion beam, however they were always present in the conducted measurements to some extent.

For the stored ions, the neutral beam is no longer present after the first reflection in the EIBT and collisions with the rear detector are significantly reduced after the first milliseconds of storage. The ions can hit the target particles, while moving in both directions in the EIBT, however the neutralized projectile can only be detected if the ion beam moves towards the neutral detector. Therefore the main source of background are the CX events, while the ion beam moves towards the front detector.

Due to the fact that the physical nature of the reaction is the same in both cases, we further discuss only the measurement with the stored ions as it has a better signal-to-noise ratio. The experimental parameters for this measurement can be found in Appendix B.

3.3.2 Time spectrum

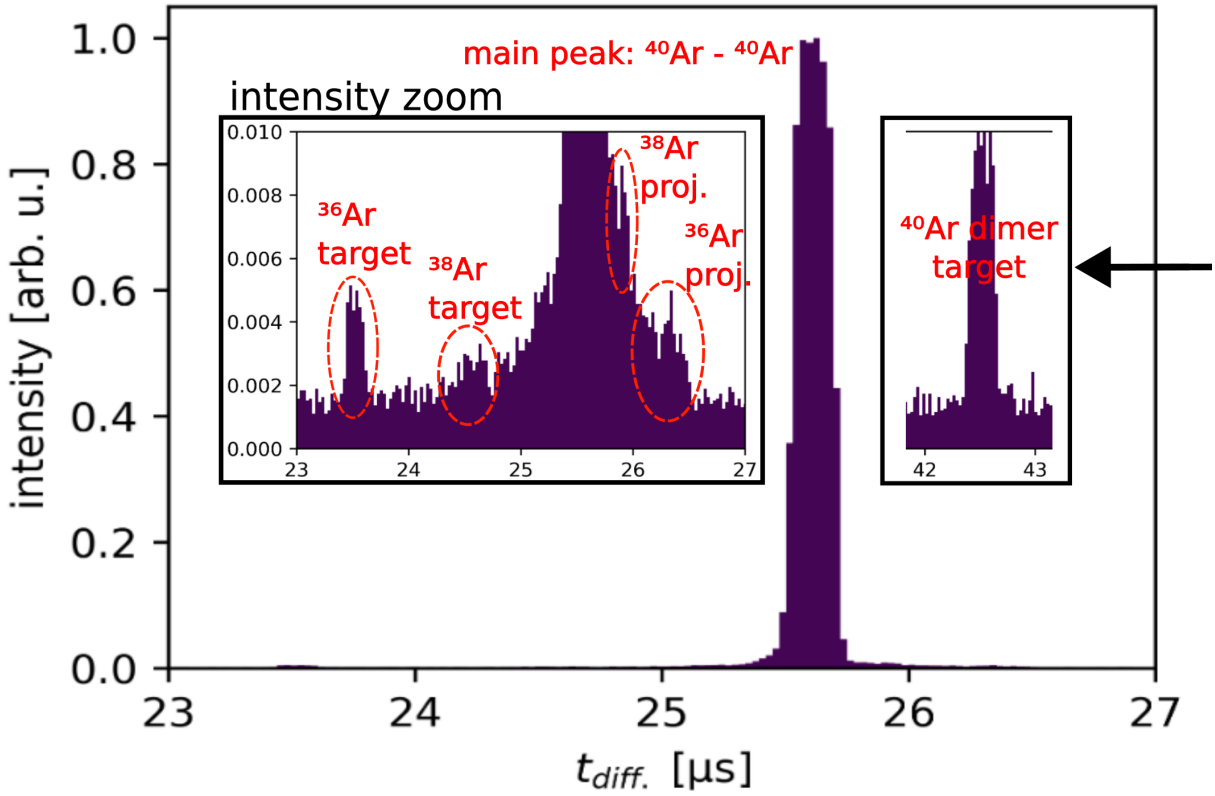

Figure 26: Time spectrum with identified peaks. Inlets depict a 100x intensity zoom. The right-side inlet depicts a later time range.

In the time spectrum (Fig. 26) we can observe the strong main peak with four weaker peaks near it and one weak peak at a later time. The only possibilities for the distinct peaks at different time values are the involvement of particles with different mass or non-resonant reactions ($Q \neq 0$). The strong peak stems from the resonant reaction involving only ^{40}Ar. The weaker peaks arise from the resonant reaction involving naturally occurring stable argon isotopes ^{36}Ar and ^{38}Ar in either the target or the projectile as well as $^{40}Ar_2$ dimers in the target (produced during the expansion in the jet). Those are expected to be present as both beams are generated from natural argon gas and no mass selection is performed for either one. It is possible that there is some minor contribution to the ^{36}Ar projectile peak from the lowest projectile excitation (projectile ion captures an electron into the second lowest available state, $Q = -11.5\,\mathrm{eV}$). The identification process is explained in Section 3.3.3, Section 3.3.4 and Section 3.3.5.

Peak positions were determined as the mean value of the two half-maximum positions of a peak. Full width at half-maximum (FWHM) is used to describe the widths of the peaks. The observed peaks are summarized in Table 1.

Table 1: Observed time spectrum peaks summary. (t. - target, p. - projectile)

peak	1	2	3	4	5	6
identification	^{36}Ar t.	^{38}Ar t.	main peak	^{38}Ar p.	^{36}Ar p.	$^{40}Ar_2$ t.
$t_{\text{diff.}}$[µs]	23.52	24.58	25.61	25.91	26.40	42.52
FWHM [µs]	0.16	0.20	0.19	unknown	0.16	0.24
relative rate	$2.9 \cdot 10^{-3}$	$1.6 \cdot 10^{-3}$	1.0	$9.1 \cdot 10^{-4}$	$2.4 \cdot 10^{-3}$	$1.1 \cdot 10^{-2}$
expectation	$3.4 \cdot 10^{-3}$	$6.4 \cdot 10^{-4}$	1.0	$6.4 \cdot 10^{-4}$	$3.4 \cdot 10^{-3}$	unknown

The relative intensities of those $t_{\text{diff.}}$ peaks were computed by integrating over a window of 400 ns around the determined peak positions and subtracting manually estimated background near the peaks (for Peak 4 due to the overlap with the main peak the window was chosen manually and is narrower: between 25.87 µs and 25.97 µs). Those should only be used for validity check of identifications, thus no error estimates are given. The intensities of the weakest peaks - 2, 4 and 5 should only be seen as estimates of the order of magnitude due to small signal-to-background ratio, especially for Peak 4. Expected rates for isotope contaminations relative to the main peak are based on the natural abundances of those isotopes [20]. As it can be seen in Table 1, the measured value for ^{36}Ar in the target matches expectation within 15%, while the other values match the order of magnitude.

From the intensity of Peak 6 we can deduce that the dimer production rate in the jet was approximately 1.1%. The actual value is probably slightly higher, because it seems that the right edge of the x-position distribution of the dimers did not fit entirely on the detector in this measurement, as can be seen in Fig. 27 in the next section.

3.3.3 Influence of the recoil ion mass on its detection position

There are differences present in the mean x-positions of the detected recoil ions between the different time peaks. Those can be attributed to the different target particle masses. The mean y-positions of the recoil ions as well as the mean x- and y-positions of the projectile do not vary between the peaks.

As it can be seen in eq. (20) the shift of the recoil ion along the x-axis is proportional to its ToF. This depends on the mass of the target particle as can be seen in eq. (12): for $\Delta p_z = 0$: $t_t \propto \sqrt{m_t - m_e}$. Therefore different target masses are shifted along the x-axis relative to the main peak, more precisely they fulfill $x(t_{\text{diff.}}) = \tilde{x} + v_{\text{jet}} t_{\text{diff.}}$ (with an arbitrary constant $\tilde{x}$; assuming only ^{40}Ar projectiles).

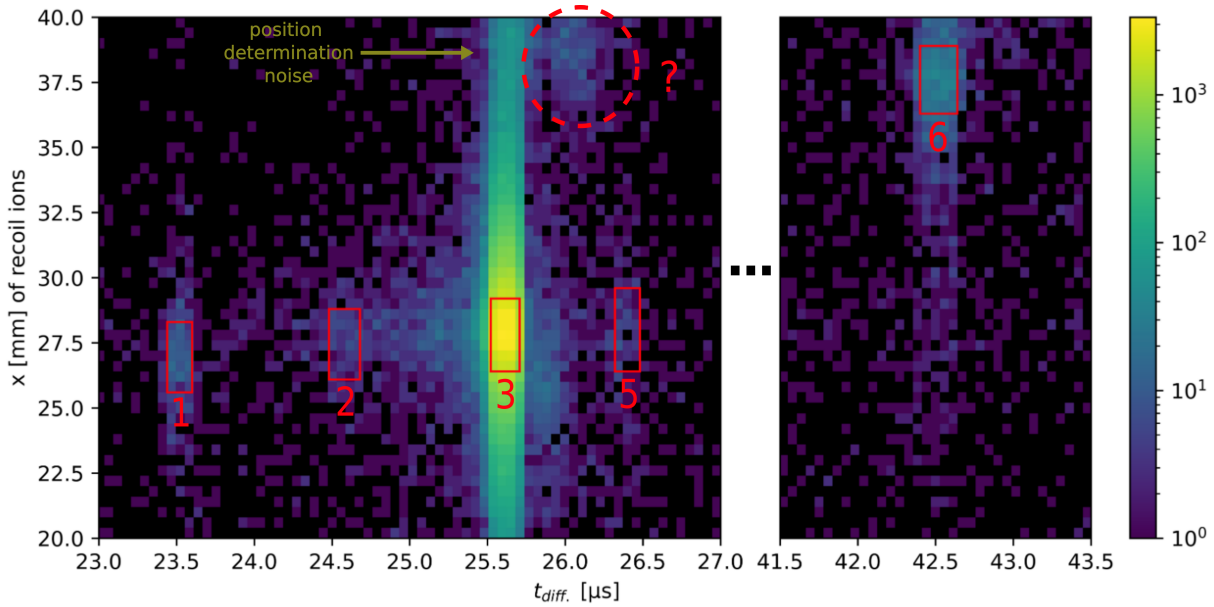

Figure 27: Time and recoil ion x-position correlation spectrum (logarithmic intensity depiction). Red boxes indicate the half-maxima positions of the distributions along either axis.

Fig. 27 shows the correlation spectrum between the time value and the x-position of the recoil ion. We can observe all the peaks from Table 1 except for Peak 4, it cannot be distinguished from the background. Additionally, there is a somewhat peculiar weak peak denoted by "?" which could not be identified. The peaks' mean x-positions and the

corresponding widths are characterised via their half-maxima positions in the x-position histograms conditioned with time windows of 400 ns around the maxima. Those are summarized in Table 2.

Table 2: The mean values and the FWHM of the x-position distributions of the recoil ions corresponding to the different time spectrum peaks.

peak	1	2	3	5	6	?
recoil ion x-pos. [mm]	27.0	27.5	27.8	28.0	37.6	38.5
FWHM [mm]	2.7	2.7	2.8	3.2	2.6	3.0

Peak 6 at significantly larger time than the main peak (Peak 3) is clearly shifted in the positive x-direction, which is strongly indicative of a heavier target. Its x-distribution did not completely fit on the detector, however both half-maxima lie well within the detector area which is sufficient for our characterization. Peak 1 at an earlier time than the main peak has a weak position shift in the negative x-direction, indicative of a smaller target mass. The shift is smaller than the widths of the x-distributions, thus its actual value is hard to determine. For the other time peaks no measurable position shift along the x-axis can be observed.

One can estimate the jet velocity from the shift of Peak 6 relative to Peak 3 to check the validity of the claim about a heavier target. Uncertainty comes mostly from the x-distribution's width, its FWHM is used for error estimation.

$$v_{\text{jet}} = \frac{x_t(\text{Peak 6}) - x_t(\text{Peak 3})}{t_{\text{diff.}}(\text{Peak 6}) - t_{\text{diff.}}(\text{Peak 3})} = (580 \pm 160)\,{}^{\text{m}}\!/\!_{\text{s}} \tag{21}$$

For comparison, according to eq. (5) the terminal flow velocity for ^{40}Ar ($\kappa = \frac{5}{3}$, $m = 39.96$ u) expanding from a room temperature (293.15 K) reservoir into the absolute vacuum is 554 $^{\text{m}}\!/\!_{\text{s}}$. Thus eq. (21) gives a plausible range, confirming the identification of Peak 6 to stem from a heavier target particle.

Peak "?" shows correlated hits on two detectors and has a comparable size to the other peaks, however we might be dealing with an artefact or noise due to lack of reasonable

explanation for it. Namely, its position is strongly shifted in the positive x-direction (to a similar extent as Peak 6) while its time is only minimally shifted. Assuming that the hits are caused by real particles: we detect a fast neutral particle behind the EIBT (can only stem from the ion beam) and a slow positive ion produced in the REMI with an initial velocity along the jet direction. The positions on the front detector however cannot be explained purely by the initial velocity inside the jet: If we assume a ^{40}Ar projectile, this would mean that the recoil ions move significantly faster than the possible maximal jet velocity. Such position shift due to a reaction recoil is also impossible, because no reaction would cause recoil strictly along a single direction almost perpendicular to the collision axis. What is left is a possibility for a combination of a heavy projectile and a heavy target, such that the corresponding time shifts almost cancel out. This can be ruled out as well: Should there be any heavier ions present in the beam, one would observe their collisions with ^{40}Ar from the jet with a much higher rate compared to the peak in question. No such signal is however observed.

Some broadening of the x-distributions might occur for larger time values due to the finite momentum distribution in the jet along its expansion direction. A non-resonant reaction might have some different momentum change distribution which could lead to a recognizably different shape of the spot in the above correlation histogram. Those effects, however, were not observed in the current experimental data.

One can also see a noise signal around the strongest peak in Fig. 27: background of randomly distributed x-positions with a sharp distribution in the time spectrum. It is briefly further examined in 3.3.6.

3.3.4 Mass contamination

The only mass contaminants expected are the less abundant stable isotopes present in the natural argon gas (^{36}Ar and ^{38}Ar) as well as Ar_n clusters formed in the jet, mainly $^{40}Ar_2$. Due to the fact that the contaminants are significantly less abundant than ^{40}Ar, reactions involving two contaminants are extremely rare. Those cannot be distinguished from the background in this measurement. Therefore we ignore reactions involving two contaminants in the following discussion. As the relative abundances of the isotopes in the ion beam are equal to those in the jet, the intensities of the peaks corresponding to the same isotope in either the target or the projectile should be equal.

Any other contamination could only arise from a leak in the gas feed to either the jet or the ion source. Should this be the case, the strongest additional signal will come from the CX of $^{14}N_2$ present in either the projectile or the target with its ^{40}Ar counterpart. No such signal was observed, thus we can rule out any peaks due to leaks.

Target

The second-strongest peak at significantly larger time (Peak 6) is indicative of a higher mass particle in the target as discussed in 3.3.3. The only such particle expected is $^{40}Ar_2$. The estimation of the mass from the shift relative to the main peak according to eq. (15) with approximate experimental parameters matches the mass of $^{40}Ar_2$ within 6%: We assume $\Delta p_z = 0$ and use expected values $d_f = 0.35\,\mathrm{m}$, $\mathcal{E} = \frac{50\,\mathrm{V}}{35\,\mathrm{cm}}$ (both subject to calibration), obtaining

$$m_t = \left((t_{\text{diff.}} - t_{\text{diff.}}(\text{Peak 3})) \sqrt{\frac{q\mathcal{E}}{2d_f}} + \sqrt{m(^{40}\mathrm{Ar})} \right)^2 \approx 75.6\,\mathrm{u} \ . \tag{22}$$

The mass calibration is then performed using the main peak and the dimer peak corresponding to the masses 39.96 u and 79.92 u [20]. From eq. (15) follows

$$\sqrt{\frac{2d_f}{q\mathcal{E}}} = \frac{t_{\text{diff.}}(\text{Peak 6}) - t_{\text{diff.}}(\text{Peak 3})}{\sqrt{m(^{40}\mathrm{Ar_2})} - \sqrt{m(^{40}\mathrm{Ar})}} = 1.585 \cdot 10^8 \, \frac{\mathrm{s}}{\sqrt{\mathrm{kg}}} \ . \tag{23}$$

Then using the obtained value we can determine the ^{40}Ar projectile ToF:

$$t_p(^{40}\mathrm{Ar}) = \sqrt{\frac{2d_f}{q\mathcal{E}}}\sqrt{m(^{40}\mathrm{Ar})} - t_{\mathrm{diff.}}(\mathrm{Peak\ 3}) = 15.22\,\mu\mathrm{s}\ . \tag{24}$$

Finally one can calculate the target mass corresponding to the time peaks (assuming ^{40}Ar projectile and $Q = 0$) using

$$m_t = (t_{\mathrm{diff.}} + t_p(^{40}\mathrm{Ar}))^2 \left(\sqrt{\frac{2d_f}{q\mathcal{E}}}\right)^{-2}\ , \tag{25}$$

the obtained values are summarized in Table 3. We can estimate the uncertainty of this determination from the width of the time peak:

$$\mathrm{FWHM}(m_t) = \mathrm{FWHM}(t_{\mathrm{diff.}}) \cdot \left|\frac{\mathrm{d}m_t}{\mathrm{d}t_{\mathrm{diff.}}}\right| = \mathrm{FWHM}(t_{\mathrm{diff.}}) \cdot 2(t_{\mathrm{diff.}} + t_p(^{40}\mathrm{Ar})) \left(\sqrt{\frac{2d_f}{q\mathcal{E}}}\right)^{-2}. \tag{26}$$

Table 3: Possible target masses corresponding to the time spectrum peaks (assuming ^{40}Ar projectile and $Q = 0$). The values assumed for the calibration are marked with *.

peak	1	2	3	4	5	6
possible target mass [u]	35.98	37.97	39.96*	40.45	41.52	79.92*
FWHM [u]	0.30	0.38	-	unknown	0.32	-

Peak 1 and Peak 2 match the masses of ^{36}Ar and ^{38}Ar (35.97 u and 37.96 u [20]) quite precisely. All the other origin possibilities for those peaks are ruled out in the further discussion and therefore they can be attributed to the mentioned isotopes in the target.

The values for Peak 4 and Peak 5 do not match any stable argon isotope, argon dimer nor $^{14}N_2$. Thus these peaks do not arise due to a target particle of a different mass.

Projectile

Using the calibrated t_p value we can calculate the corresponding projectile mass for the peaks (assuming ^{40}Ar target and $Q = 0$):

$$m_p = \left(\frac{t_{\text{diff.}}(\text{Peak 3}) + t_p(^{40}\text{Ar}) - t_{\text{diff.}}}{t_p(^{40}\text{Ar})} \right)^2 m(^{40}\text{Ar}) \ , \tag{27}$$

the obtained values are summarised in Table 4. The uncertainty can be estimated from the peak's width (ignoring uncertainty in $t_p(^{40}\text{Ar})$ calibration):

$$\begin{aligned} \text{FWHM}(m_p) &= \text{FWHM}(t_{\text{diff.}}) \cdot \left| \frac{\mathrm{d}m_p}{\mathrm{d}t_{\text{diff.}}} \right| \\ &= \text{FWHM}(t_{\text{diff.}}) \cdot 2 \frac{t_{\text{diff.}}(\text{Peak 3}) + t_p(^{40}\text{Ar}) - t_{\text{diff.}}}{t_p(^{40}\text{Ar})^2} m(^{40}\text{Ar}) \ . \end{aligned} \tag{28}$$

Table 4: Possible projectile masses corresponding to the $t_{\text{diff.}}$ peaks (assuming ^{40}Ar target and $Q = 0$). The value assumed for the calibration is marked with *.

peak	1	2	3	4	5	6
possible proj. mass [u]	51.69	45.55	39.96*	38.40	35.91	0.49
FWHM [u]	0.96	1.12	-	unknown	0.80	0.14

Here only Peak 4 and Peak 5 yield reasonable values, corresponding to ^{38}Ar (37.96 u) and ^{36}Ar (35.97 u). Peak 4 is difficult to characterize and properly identify due to its strong overlap with the edge of the main peak. However, judging by the presence and the intensity of the ^{38}Ar target peak as well as the rough match with the expected $t_{\text{diff.}}$, it stems most probably from ^{38}Ar projectiles. Peak 5 can also contain some certain non-resonant CX events as shown in 3.3.5. Nevertheless, it can be mostly attributed to the reactions with ^{36}Ar projectiles, because the corresponding count rate should be equal to the reactions with ^{36}Ar in the target and Peak 3 corresponding to the latter is even slightly stronger than Peak 5.

The values for Peak 1 and Peak 2 do not match neither any stable argon isotopes nor $^{14}N_2$, thus their origin from reactions with other projectiles than ^{40}Ar can be ruled out.

3.3.5 Non-resonant reactions

Finally we can check for the non-resonant reactions. The main peak gives the $t_{\text{diff.}}$ value corresponding to $Q = 0$ as a reference. It is, however, impossible to calibrate the gradient $\frac{\mathrm{d}Q}{\mathrm{d}t_{\text{diff.}}}$ as it requires an identified peak with a non-zero Q-value. Thus in order to check whether one of the peaks could correspond to such non-resonant CX, we estimate the gradient according to eq. (18), assuming $E_0 = 2\,\text{keV}$, $m_p = m_t = 39.96\,\text{u}$ and $\mathcal{E} = \frac{50\,\text{V}}{35\,\text{cm}}$, $d_n = 1.5\,\text{m}$,

$$\frac{\mathrm{d}Q}{\mathrm{d}t_{\text{diff.}}} = -\sqrt{\frac{2E_0}{m_p}}\left(\frac{1}{q\mathcal{E}} - \frac{m_p}{m_t}\cdot\frac{d_n}{2E_0}\right)^{-1} = -14.8\,\frac{\text{eV}}{\mu\text{s}} \quad . \tag{29}$$

We can then estimate the possible Q-values corresponding to the peaks using

$$Q = \frac{\mathrm{d}Q}{\mathrm{d}t_{\text{diff.}}}\cdot\left(t_{\text{diff.}} - t_{\text{diff.}}(\text{Peak 3})\right) \quad , \tag{30}$$

the obtained values are summarized in Table 5.

In order to estimate the corresponding resolution we use the FWHM of the main peak (other peaks have similar widths) and the estimated value of $\frac{\mathrm{d}Q}{\mathrm{d}t_{\text{diff.}}}$

$$\text{FWHM}(Q) = \text{FWHM}(t_{\text{diff.}})\cdot\left|\frac{\mathrm{d}Q}{\mathrm{d}t_{\text{diff.}}}\right| \approx 2.8\,\text{eV} \quad . \tag{31}$$

Table 5: Possible Q-values corresponding to the $t_{\text{diff.}}$ peaks (assuming ^{40}Ar target and projectile). The value assumed for the calibration is marked with *.

peak	1	2	3	4	5	6
Q-value [eV]	31.0	15.3	0*	-4.5	-11.6	-250.2

A vast majority of the projectile and the target atoms can be assumed to be in their electronic ground state before the collision, thus only excitations can occur ($Q < 0$). The most probable excitations are those of the neutralized projectile (electron captured not in the lowest available 3p but into a 4s or higher orbital up to Ar^+ continuum) and lie in the range between 11.5 eV and 15.8 eV [11], corresponding to the same negative range

in Q-value. The possible target excitations lie in the range between 13.5 eV and 27.6 eV (instead of the ground state configuration [Ne]$3s^2 3p^5$, the recoil ion is in [Ne]$3s3p^6$ or a higher state up to Ar^{2+} continuum) [11]. Even less probable simultaneous excitations of both projectile and target would lie in the range between 25.0 eV and 43.4 eV.

The only reasonable candidate for a non-resonant reaction in Table 5 is Peak 5, corresponding to the first projectile excitation (electron captured into the 4s orbital, $Q = -11.5\,\mathrm{eV}$). This however can be mostly attributed to ^{36}Ar projectiles, as discussed in 3.3.4. Nevertheless, some contribution from the projectile excitation cannot be ruled out.

As expected the resolution is strongly limited by the target thickness. We can estimate the maximal jet width along z-axis (FWHM) using eq. (19) (assume $d_f = 0.35\,\mathrm{m}$, $d_f = 1.5\,\mathrm{m}$, $\mathcal{E} = \frac{50\,\mathrm{V}}{35\,\mathrm{cm}}$, $E_0 = 2\,\mathrm{keV}$, $m_t = m_p = 39.96\,\mathrm{u}$):

$$\mathrm{FWHM}(d_f) \leq \mathrm{FWHM}(Q) \cdot \sqrt{\frac{m_p q \mathcal{E} d_f}{m_t E_0}} \left(\frac{1}{q\mathcal{E}} - \frac{m_p d_n}{2 m_t E_0} \right) \approx 2.9\,\mathrm{mm} \ , \tag{32}$$

which is in accordance with the estimation in eq. (10).

3.3.6 Position distributions

In Section 3.3.3 the mean positions corresponding to the different $t_{\text{diff.}}$ peaks were discussed. Here the shape of the spatial distribution around this mean value is discussed. As no non-resonant reactions between ^{40}Ar could be extracted, only the position distributions of the strongest peak are presented (selected via 400 ns time window condition), see Fig. 28.

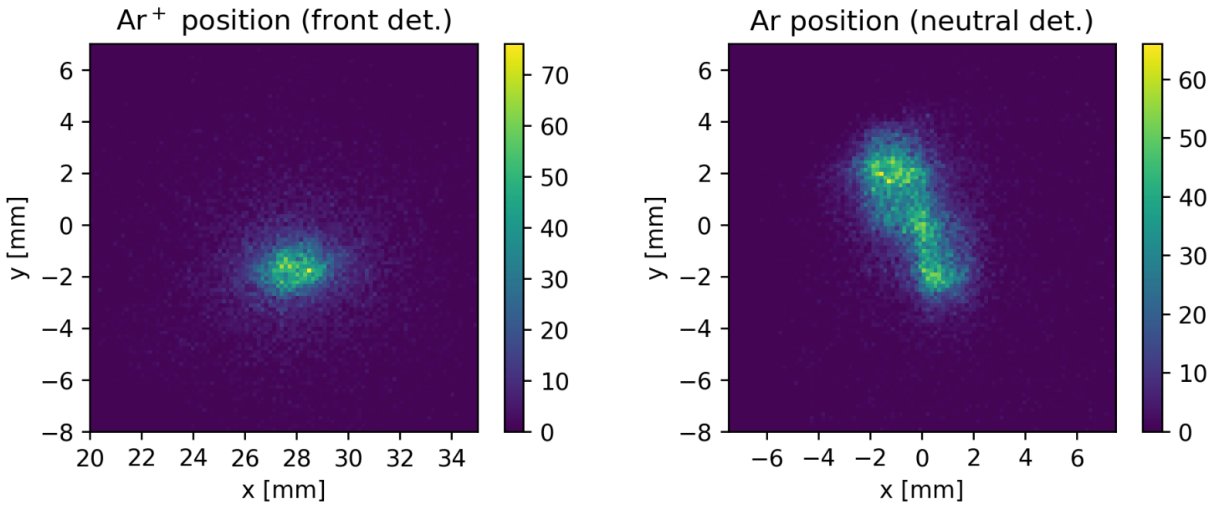

Figure 28: Position distributions of the coincident hits from the main time spectrum peak.

Recoil ion

Such a distribution could in principle be used to reconstruct the transversal momentum distribution, however here the final distribution on the detector is of almost the same size as the expected reaction site size (see eq. (10)). Therefore it is impossible to separate the momentum from the initial position. We can, however, give an upper limit on the widths of all the distributions contributing to the final position. The FWHM of the final x- and y-position distributions is used for it.

The width of the x-position distribution is composed of the ion beam x-width FWHM(x_0), width of the velocity distribution in the jet FWHM(v_{jet}) and the momentum change in the reaction Δp_x, thus

$$\mathrm{FWHM}(x_0) \leq \mathrm{FWHM}(x_t) = 2.8\,\mathrm{mm}\ , \tag{33}$$

$$\mathrm{FWHM}(v_{\mathrm{jet}}), \frac{\mathrm{FWHM}(\Delta p_x)}{m(^{40}\mathrm{Ar})} \leq \frac{\mathrm{FWHM}(x_t)}{t_{\mathrm{diff.}} + t_p} = 68\,\frac{\mathrm{m}}{\mathrm{s}} = \frac{2.3\,\mathrm{a.u.\ (mom.)}}{m(^{40}\mathrm{Ar})}\ . \tag{34}$$

The width of the y-position distribution is composed of the beams' overlap y-width $\mathrm{FWHM}(y_0)$, width of the transversal velocity distribution in the jet $\mathrm{FWHM}(v_{\mathrm{jet},\perp})$ and the momentum change after the reaction Δp_y, thus

$$\mathrm{FWHM}(y_0) \leq \mathrm{FWHM}(y_t) = 3.2\,\mathrm{mm}\ , \tag{35}$$

$$\mathrm{FWHM}(v_{\mathrm{jet},\perp}), \frac{\mathrm{FWHM}(\Delta p_y)}{m(^{40}\mathrm{Ar})} \leq \frac{\mathrm{FWHM}(y_t)}{t_{\mathrm{diff.}} + t_p} = 78\,\frac{\mathrm{m}}{\mathrm{s}} = \frac{2.6\,\mathrm{a.u.\ (mom.)}}{m(^{40}\mathrm{Ar})}\ . \tag{36}$$

Projectile

The final position distribution is indicative of a complicated not cylindrically symmetrical momentum distribution in the stored ion beam overlapping with the jet. One could further optimize this position distribution on the neutral detector to a small round spot in order to improve the transversal momentum determination. That would be indicative of a narrower cylindrically symmetrical initial transversal momentum distribution in the ion beam, meaning a better-defined collision axis.

Noise/Background

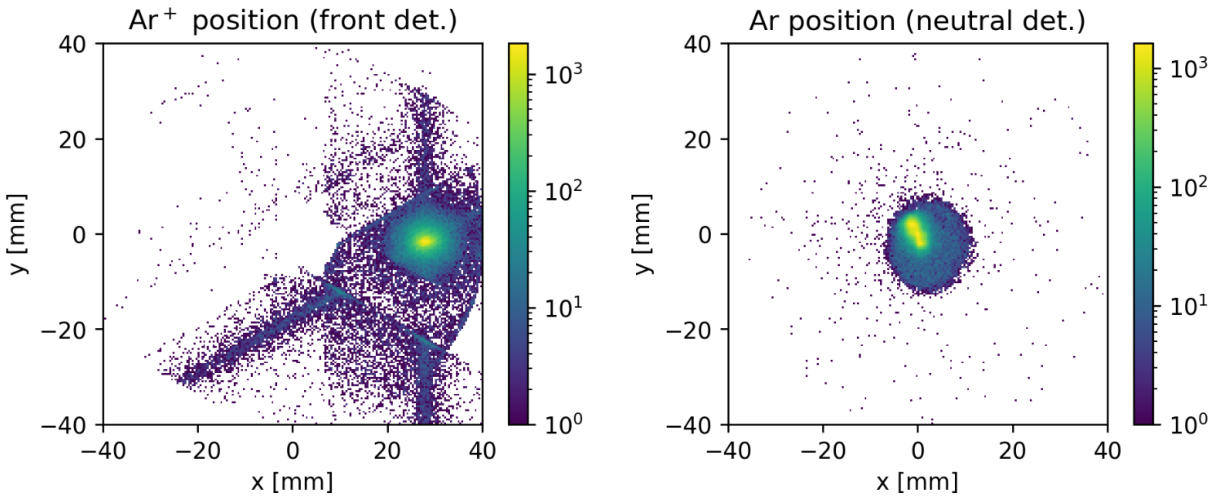

Figure 29: Position distributions for the main $t_{\text{diff.}}$ peak in logarithmic depiction (same data as in Fig. 28).

As can be seen in Fig. 29 the measured position distribution on the front detector contains some low-rate noise with a specific shape. This is the same noise as the stripe along x-position in Fig. 27 in section 3.3.3. One can see stripes going through the strong spot of actual recoil ion positions parallel to the delay lines' winding directions along the whole detector. This noise probably arises from false position determination along one delay line, while the position along the second one is correct. The errors could occur in the position determination algorithm in the primary data evaluation, if for one delay line some signal not stemming from the same hit as the rest is used. The exact origin could not be identified.

The distribution on the neutral detector seems to only have the background of some particles accidentally matching the coincidence condition. The particles mostly stem from the REMI chamber, thus most background counts lie in a circle determined by the rear detector hole.

3.3.7 Ion beam temporal evolution

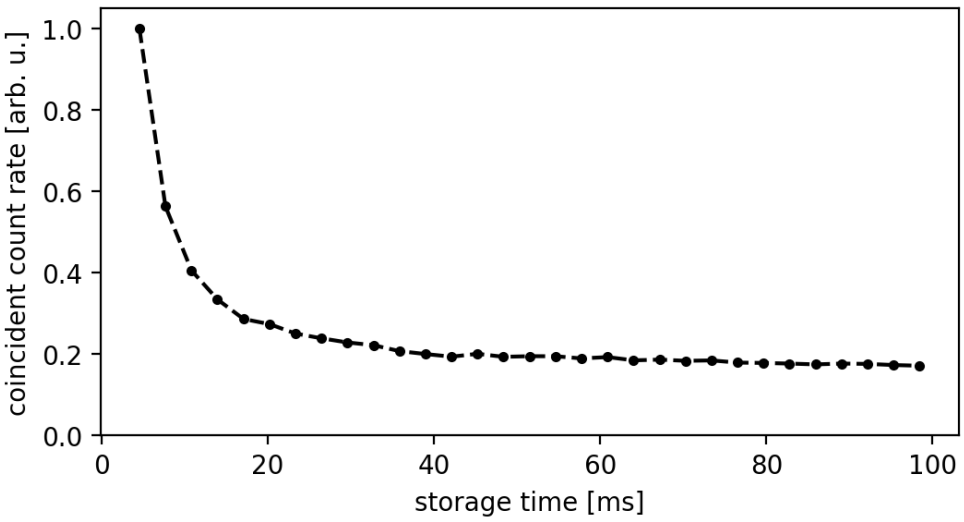

Figure 30: Temporal evolution of the coincident (Peak 3) count rate.

Measuring the temporal evolution of the coincident count rate provides a direct measure of the relative ion density evolution. This is plotted for the discussed measurement in Fig. 30. Here the count rates were calculated by integrating the strongest $t_{\text{diff.}}$ peak (400 ns window) for 30 equal slices in storage time between 3 ms and 100 ms.

The ion density drops in a rather fast over-exponential manner for the first few 10 ms and then decreases significantly slower afterwards. The results are similar to the previously conducted observations of the ion density evolution [27]. If one aims for a higher count rate, it is beneficial to only conduct experiments during the first couple of 10 ms. On the other hand, one can reduce the maximal count rate without changing any experimental parameters, if needed, by starting the data recording at a somewhat later storage time. Too high count rates can overflow the buffer of the data acquisition system, causing dead time.

It was also observed that the average beam shape and velocity distribution (over several oscillations in EIBT) do not change with storage time. For that, the position distributions corresponding to the strongest $t_{\text{diff.}}$ peak were compared for different storage time slices. No distinguishable difference was noticed.

3.4 Remarks for future ion-atom/molecule experiments

3.4.1 Detection scheme expansion possibilities

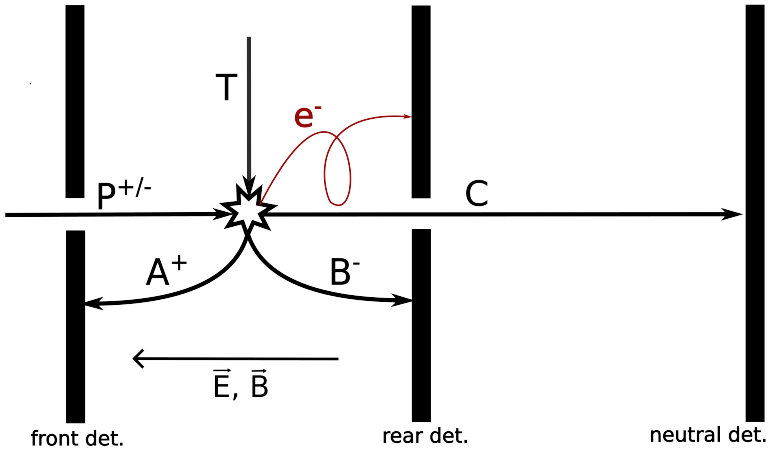

Figure 31: Scheme of fragments, that can be detected in ion-atom/molecule collisions in TrapREMI. P - projectile, T - target, A^+, B^- - charged target fragments, C - neutral projectile fragment, e^- - electron from either target or projectile.

Future experiments might include some fragments of other types than detected in this work. Figure 31 gives an overview of what particles can be detected after a reaction induced by crossing an ion beam with a gas jet in the TrapREMI. Note that one can also detect several fragments of the same type simultaneously.

In the implemented detection scheme for CX positive fragments of the target as well as neutral fragments from the projectile have already been detected. It can be further expanded with the detection of electrons detached from either the target or the projectile. The electron detection has not been tested in TrapREMI to date, however all the prerequisites for this detection are met. Should there be any heavy negative fragments from the target (very unlikely in achievable collision energy range), those can be detected on the rear REMI detector in analogy to the positive fragments. Neutral target fragments cannot be detected.

Charged projectile fragments cannot in general be detected due to their high longitudinal momentum. They could only be detected in case of reactions with high transversal momentum gain.

3.4.2 Resolution improvement via time-focusing

The main problem witnessed in the test experiment was the limited longitudinal momentum (and thus the Q-value) resolution due to the target thickness. This section describes a method to significantly improve it. This method would require rewiring of the REMI electrodes and was not feasible for this work.

One can focus different longitudinal reaction positions on a narrow time spectrum range without reducing the momentum sensitivity, as long as the position spread is small compared to the mean distance to the detector. A possible way to do that is to accelerate recoil ions with a homogeneous electric field for $\frac{1}{3}$ of the distance to the detector and let them drift without acceleration for the rest of the distance [4]. This can be achieved with our REMI stack of 30 electrodes by setting electrodes 1-10 (counting from the front detector side) to some negative potential $-U$, electrodes 20-30 at U and create a homogeneous potential ramp from $-U$ to U with electrodes 10-20. To implement this, one needs to open the REMI chamber, remove the voltage divider from the electrode stack and add individual feedthroughs for each electrode.

The measurable time $t_{\text{diff.}} = t_t - t_p$ can be calculated the same way as in eq. (15) adding a drift with constant velocity

$$v_{\text{drift}} = \sqrt{\frac{2q\mathcal{E}(\frac{1}{3}d_f + \Delta z)}{m_t}} - \frac{\Delta p_z}{m_t} \ . \tag{37}$$

We include a shift in the initial position Δz to the calculation, make the assumption of small Δp_z in analogy to eq.(15) and account only for the linear contributions.

$$t_t = \sqrt{\frac{2m_t(\frac{1}{3}d_f + \Delta z)}{q\mathcal{E}}} + \frac{\frac{2}{3}d_f}{\sqrt{\frac{2q\mathcal{E}}{m_t}(\frac{1}{3}d_f + \Delta z)}} - \frac{\Delta p_z}{q\mathcal{E}}\left(1 + \frac{d_f}{d_f + 3\Delta z}\right) \ , \tag{38}$$

$$t_p = \frac{d_n - \Delta z}{\sqrt{\frac{2(E_0 - q\mathcal{E}\Delta z)}{m_p}}} - \frac{(d_n - \Delta z)m_p}{2(E_0 - q\mathcal{E}\Delta z)m_t}\Delta p_z \ . \tag{39}$$

The sensitivity for Δp_z in $t_{\text{diff.}}$ rises compared to the currently implemented homogeneous extraction field (see eq. (15)) (ignore small Δz contributions):

$$\left.\frac{\mathrm{d}t_{\text{diff.}}}{\mathrm{d}\Delta p_z}\right|_{\Delta p_z = 0} = \frac{2}{q\mathcal{E}} - \frac{d_n m_p}{2E_0 m_t} \ . \tag{40}$$

The second term is usually at least one order of magnitude smaller, meaning that the sensitivity increases almost two times. This corresponds to a two-fold increase in Q-value sensitivity (assuming linear approximation in analogy to eq. (17)).

The choice of the length ratio between the acceleration and the drift part ensures

$$\left.\frac{\mathrm{d}t_t}{\mathrm{d}\Delta z}\right|_{\Delta z = 0} = 0 \tag{41}$$

as it can be easily confirmed by taking a derivative of eq. (38) with respect to Δz. This means no first order contribution to the target ToF from the position spread. Higher order contributions as well as the influence on the projectile ToF remain. We can estimate the remaining time spread due to the position uncertainty by calculating the difference between $t_{\text{diff.}}$ for $\Delta z = \pm 1.45\text{mm}$ (corresponds to the jet width estimated in eq. (32)) using eq. (38) and (39) (ignore small contribution from Δp_z).

$$t_{\text{diff.}}(\Delta z = 1.45\text{mm}) - t_{\text{diff.}}(\Delta z = -1.45\text{mm}) = 30\,\text{ns} \ . \tag{42}$$

The above value is ca factor 6.7 smaller than in the observed time peaks and corresponds to a Q-value uncertainty width of ca 0.2 eV (using the estimation in eq. (29) and assuming the two-fold increase in Q-value sensitivity). The only relevant contribution to the time peak width comes from the projectile ToF spread. Note that the initial momentum spread is not accounted for in this estimation.

3.4.3 Projectile mass selection via kick-out in EIBT

As it was seen in the experiment, contaminations of unwanted masses might create additional peaks in the time spectrum. While there is no simple method for mass selection in the gas jet target in the current setup, the projectile mass can be selected using the EIBT. It might be especially useful if the ions of interest are not the ones produced with the highest yield in the ion source (e.g. H_3^+ from H_2 gas).

One can use the so-called kick-out mass selection technique [30]. It is based on the fact that the oscillation period in the EIBT is proportional to the square-root of mass, and requires only an electrode capable of kicking ions out of the trap, located in the high-velocity region of the EIBT. In TrapREMI one of the EIBT steerer electrodes can be used.

This electrode can be set to some high potential, blocking ions from getting trapped. However, if it is switched to zero, ions can pass without disturbance. This potential can be used to enforce a certain condition on the storage: only ions passing the kick-out site during an allowed time interval (zero potential) are stored. During the injection of the ion beam, a time window of Δt is opened (zero potential), and for the rest of the time the ions are kicked out. This procedure defines the temporal structure of the stored beam - a bunch is created. The time window is then reopened with a periodicity of T_0 equal to the oscillation period corresponding to the wanted mass m_0. After n oscillations only the ions with an oscillation period T in the following range are left:

$$T = T_0 \pm \frac{\Delta t}{n} \ . \tag{43}$$

This corresponds to the mass range of (linearized in $\frac{\Delta t}{T_0}$)

$$m = m_0 \pm \frac{2m_0\Delta t}{nT_0} \ . \tag{44}$$

The allowed mass window can be decreased by decreasing Δt or waiting for more oscillations.

4 Test of an ion bunching technique

4.1 Basics of RF-bunching

Radio-frequency (RF) bunching is a technique for creating or maintaining longitudinal ion bunches in electrostatic ion storage devices. It was already implemented in several EIBT experiments (e.g. [6], [5]).

The dispersion relation, i.e. the relation describing the dependence of the oscillation period T in the EIBT on the storage energy E_0, is an important characteristic of a trapping potential. In general, ion bunches disperse in the EIBT due to some initial spread in their kinetic energy. In case of negative $\frac{\mathrm{d}T}{\mathrm{d}E_0}$ slower ions move to the rear part of the bunch and start lagging behind over time, while faster ions rush ahead of the bunch. Overall, the bunch broadens and its structure is lost after some time. In case of positive $\frac{\mathrm{d}T}{\mathrm{d}E_0}$ bunches disperse with a reversed velocity distribution.

The RF-bunching is performed by applying a weak sine potential, resonant to the ion oscillation, at a single position in the EIBT. The amplitude is typically order 10^3 lower than the storage energy per elementary charge. The name of the method comes from the fact that the oscillation frequencies in electrostatic storage devices lie in the RF range.

Fig. 32 illustrates the working principle of RF-bunching for a negative $\frac{\mathrm{d}T}{\mathrm{d}E_0}$. If we were to ignore the acceleration due to the RF-signal and the kinetic energy spread, the ions would arrive at exactly the same phase of the sine. When ions arrive in the bunching region at the falling edge of the bunching potential, they get decelerated and thus arrive at a slightly later sine phase during the next round-trip. On the rising edge they experience acceleration and shift towards an earlier phase of the sine. Overall, the ions collect themselves at the stable minimum of the sine creating a sharp bunch. In case of positive $\frac{\mathrm{d}T}{\mathrm{d}E_0}$ the bunch would collect itself at the maximum of the sine. Should there be a minor mismatch in the frequencies, the average ion storage energy is shifted to match the bunching frequency.

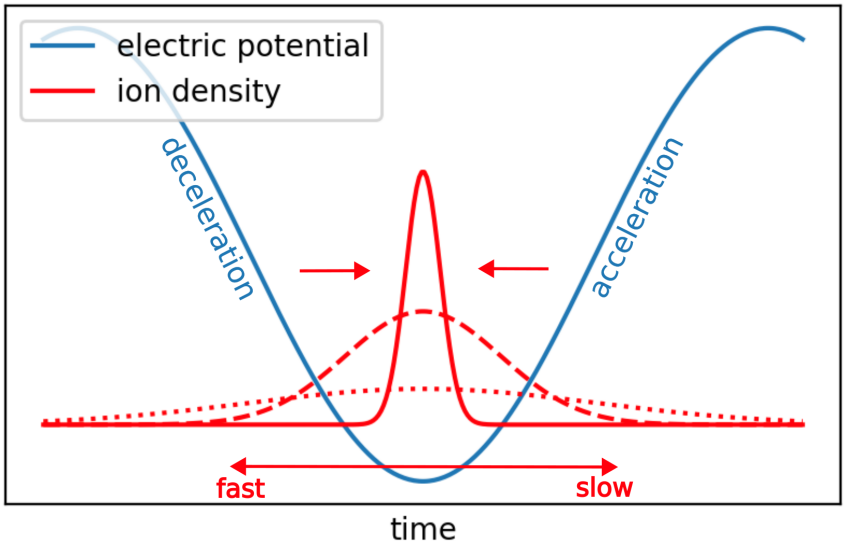

Figure 32: RF-bunching working principle for negative $\frac{\mathrm{d}T}{\mathrm{d}E_0}$.

Note, that the exact dynamics is more complicated due to the Coulomb interaction between the stored ions. It plays a role in the dynamics of the momentum and position distribution inside an ion bunch [8] and may influence the bunch dispersion [18] and thus the required conditions for the RF-bunching.

In an EIBT bunching is usually performed somewhere in the region between the two mirrors, which is passed through twice during one oscillation. Therefore two bunches can arise while travelling in opposite directions. In this work bunching at a reverse point in an EIBT mirror was tested. This position is traversed only once per oscillation period.

Potential use cases in the TrapREMI

A possible practical purpose for creation of the ion bunches from inside the EIBT in our setup would be to compress a continuous ion beam into a higher density bunch. It might be useful if the ion source can only produce a dilute beam and the signal is otherwise weak compared to the background. One could then perform a temporal selection in the data analysis such that only the reaction times when the ion bunch passes the interaction region are accounted for. The bunch generation for this purpose should occur as fast as possible, while stability over long timescales is not a priority (usually a goal of the bunching in other EIBT experiments). Longer storage timescales are less interesting in TrapREMI due to the significant ion density loss during the storage and the corresponding reaction rate decrease.

Another possible use for the ion bunching is to define a sharp reaction time in collision experiments by creating a very short ion pulse. In order to use this reaction time for the momentum reconstruction, the temporal width of the bunch must be maximally of the order of the time uncertainties caused by other experimental limitations (e.g. maximally a few 10 ns in case of the discussed ion-atom collisions with time-focusing). To achieve such a narrow bunch, one should start by injecting an initially short bunch and then further compress it. It was not tested whether that sharp bunches are achievable in our EIBT.

4.2 Test in the TrapREMI device

The test measurement was performed by filling almost the entire trap with ions and applying a periodical bunching potential to a single EIBT electrode with an arbitrary waveform generator. The EIBT cannot be filled entirely due to the nature of the ion injection procedure in the TrapREMI setup. The ion beam temporal density at a single position was tracked via counts on one of the REMI detectors during the whole storage cycle of 100 ms.

First an innermost (nearest to the REMI) EIBT stack electrode was used for bunching and different RF-field parameters were tested. In all the measurements the ion density moved between the two possible bunch positions and no stable configuration could have been found. The existence of suitable bunching parameters, however, cannot be fully ruled out as no systematic study of the full possible parameter space was conducted.

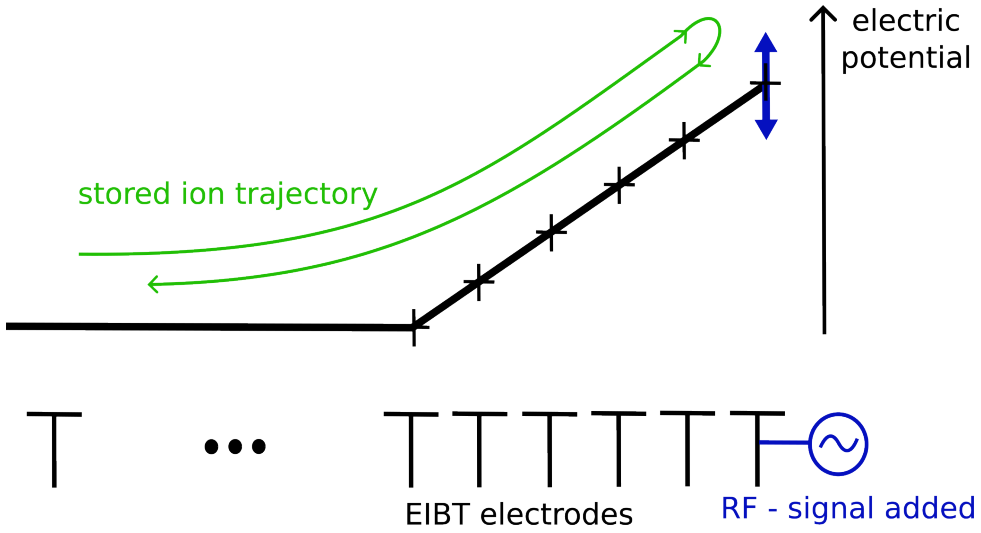

Figure 33: Sketch of the bunching potential position for the presented experimental results. The weak alternating potential is added on top of the high voltage potential of the last mirror electrode. The reverse point of the stored ions is between the last two mirror electrodes.

Next, the outermost mirror electrode was used for bunching, see Fig. 33. This is the only position which is passed only once per oscillation period, thus only one bunch is created. This removes the influence on the bunch passing the bunching region at a “wrong” sine

phase while moving in one of the two directions. On the other hand, it is the region of low velocity and thus high longitudinal density, which may influence the efficiency of the bunching and increase trap losses due to Coulomb repulsion. Another concern is that faster ions experience a stronger bunching field than their slower counterparts, as they travel deeper into the mirror. Additionally, the amplitude of the optimal bunching potential should also depend on the ion turnaround position determined by the mirror potential height.

In the following the best bunching achieved using the outermost mirror electrode is presented (again no systematic study of the full parameter space was conducted). A sine signal of 26.560 kHz and 7.5 V amplitude was used to bunch ions stored at 2.5 keV between mirrors of 3.2 kV. Full experimental settings can be found in Appendix C. Fig. 34 depicts the observed signal: measured count rate on a REMI detector over 100 µs windows is presented for different storage times between 2 ms and 26.1 ms. In this signal peaks appear with the periodicity of ca 38 µs equal to the oscillation period in the EIBT (indicative of a single bunch in the EIBT).

Data recording was started at 2 ms and some initial bunch formation can already be observed from the beginning. The observed bunch sharpens over time, reaching its sharpest shape (FWHM ca 1 µs) at ca 11 ms. Afterwards it decays, becoming significantly less sharp by 20 ms and by 22 ms almost no structure can be seen. Exact reasons for bunch decay could not be identified. This rather short time of bunch stability, however, would probably be sufficient for uses cases in TrapREMI. Periodical dips in the counts are present due to the ion density gap from the injection procedure.

Should one want to employ this bunching scheme in an experiment in the future, one would need to do some further planning, optimization and explore the bunching possibilities for the experiment in question. It was however shown, that the ion beam compression into a bunch in TrapREMI is in principle possible at timescales under 10 ms.

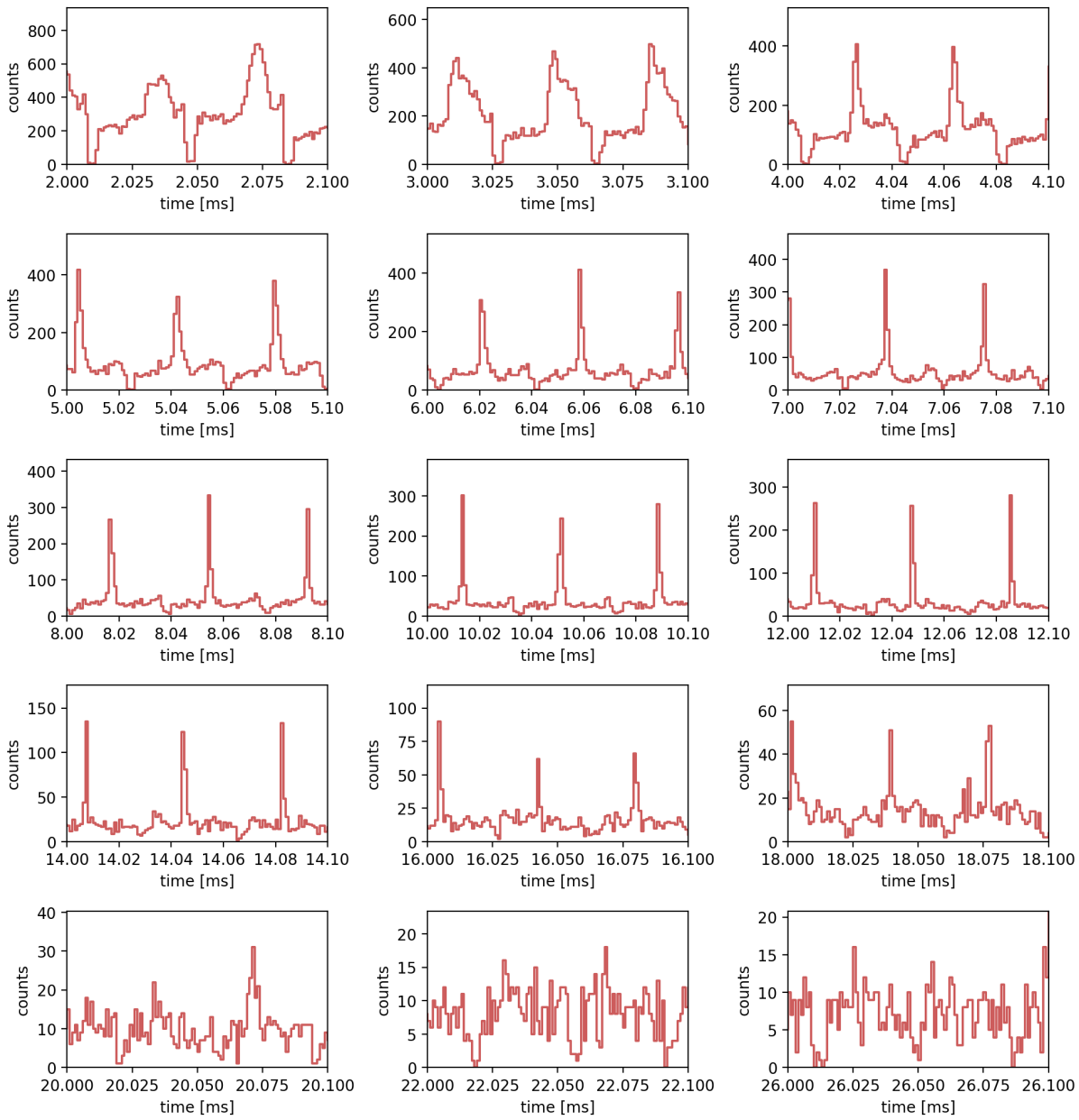

Figure 34: Counts on the rear REMI detector during RF bunching.

5 Summary

The broader goal of the TrapREMI device is to study dynamics of (molecular) ions. Those play an important role in gas-phase chemical processes in different natural environments e.g. atmospheres or the interstellar medium. This work focused mainly on the implementation of the collision experiments between ions and atoms (molecules can be used as a target in an analogeous way).

For this purpose a gas jet setup was assembled. It utilizes expansion through a microscopic nozzle to create a cold directed gas beam. This beam serves as a target in collision experiments with ions in the reaction microscope. Some minor updates were also done to the pre-existing setup: A new ion source was acquired and installed to provide a possibility of a higher ion current as well as negative ion production. Control of the electrode voltages via a PC software was implemented for a faster and more intuitive operation.

In order to test the feasibility of ion-atom collision experiments in the TrapREMI setup, a simple reaction with a high cross-section was observed: A singly-charged argon ion captures an electron from a neutral argon atom at 2 keV collision energy. Both reaction products were successfully detected in coincidence on two separate detectors. It was also observed that the measurements performed with the ion beam stored in the EIBT had less background signal than when performed with a direct beam without storage. Naturally occurring argon isotopes ^{36}Ar and ^{38}Ar in both the ion beam and the jet could be observed in the experimental data with order $10^2 - 10^3$ times lower abundances compared to ^{40}Ar. It was also observed that approximately 1.1% of the particles in the jet were argon dimers produced due to cooling. Non-resonant electron capture events could not be distinguished. Momentum changes orthogonal to the collision axis were below the resolution limit imposed by the reaction volume size to be measured. The Q-value uncertainty in the experiment was estimated to be 2.7 eV which is rather high for this type of experiment. The main contribution to this uncertainty comes from the width of the jet. Overall, it was shown that the TrapREMI setup can be used to study ion-atom/molecule collisions after a minor improvement and the jet setup works properly.

The Q-value (reaction energy) resolution can and should be significantly improved in the near future via the so-called time-focusing, which was already successfully implemented in REMI experiments pre-dating this work, e.g. [31]. For this purpose the REMI electrodes should be rewired to allow a somewhat different extraction potential. The typically used form of the potential was discussed in Section 3.4.2. It was estimated to improve the Q-value resolution for the discussed experiment by ca factor 13. Should one need to implement mass selection in the ion beam, it can be done in a straightforward manner via so-called kick-out mass selection from inside the EIBT.

Additionally, a technique for longitudinal compression of the ion beam into a sharp bunch while stored in the EIBT was briefly experimentally explored. In the best achieved configuration the ion beam filling almost the entire EIBT was compressed into a sharp bunch after ca 6 ms, it then started decaying after another ca 10 ms, losing its structure almost completely after ca 22 ms of total storage time. Should one need short ion bunches with a higher density for a REMI experiment, this technique can be used. Its use would, however, require some further planning, testing and optimization.

A EIBT and REMI electrode scheme

The following Fig. 35, 36, 37 depict the electrodes in the EIBT and the REMI. The box labelled "HV switch" depicts a fast high voltage switch used for the ion injection procedure. All the other labelled boxes depict a voltage supply connected to an electrode. If not indicated otherwise the electrodes are grounded.

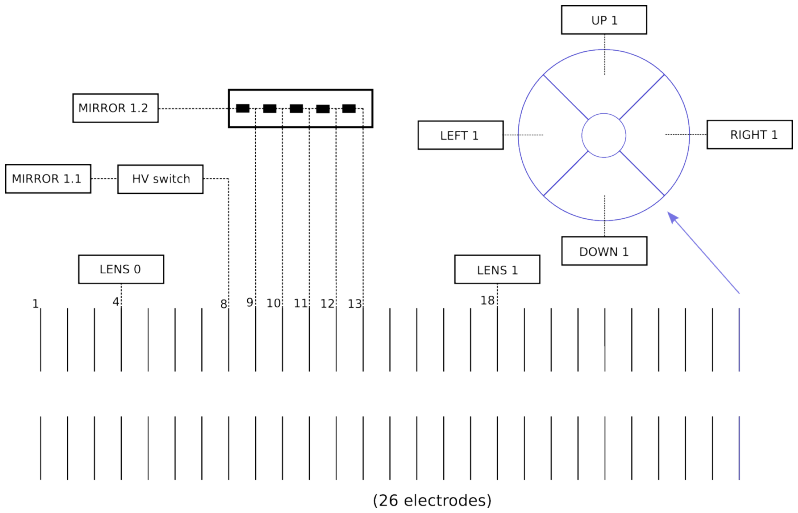

Figure 35: Electrode scheme of the EIBT entrance side stack.

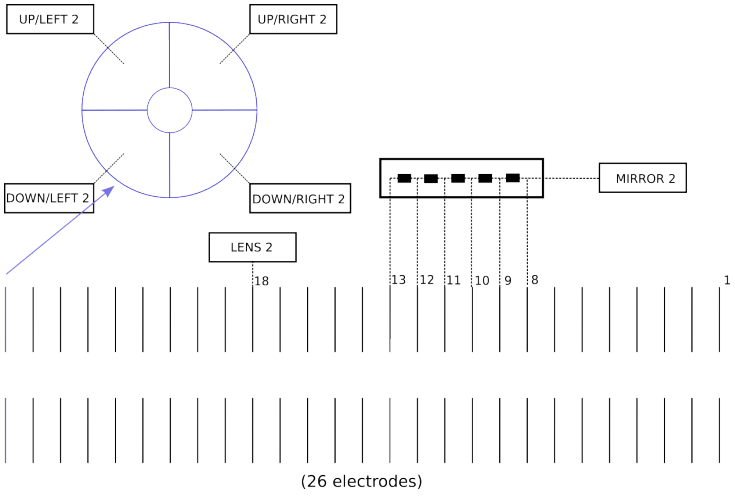

Figure 36: Electrode scheme of the EIBT exit side stack.

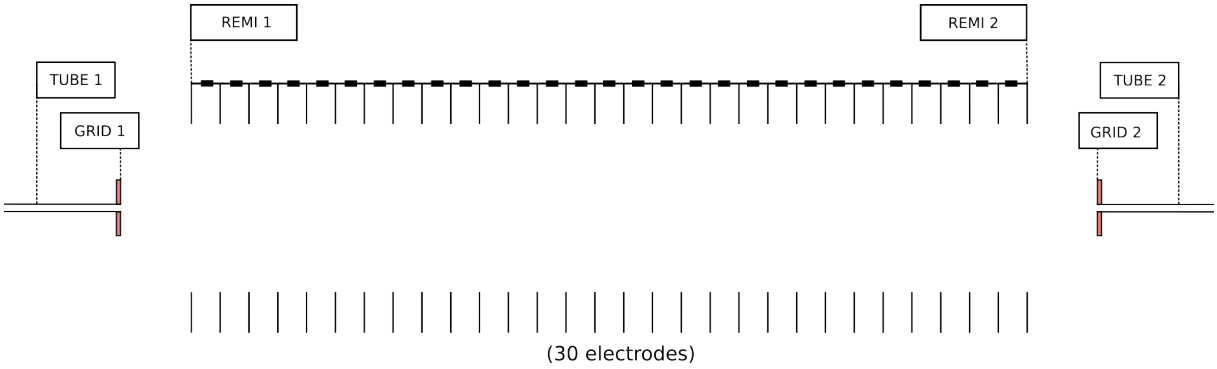

Figure 37: Electrode scheme of the REMI. The electrodes are connected in a row with equal resistors between the neighboring electrodes.

B Experimental settings for the collision experiment

The experimental settings for the argon symmetric CX experiment with stored ions are listed in this appendix: Table 6 summarizes the settings of the ion source, the electrode stack directly after it and the 90°-deflector. "LENS" refers to the einzel lens and "UP", "DOWN", "LEFT", "RIGHT" refer to the four electrodes of the 4-quadrant-steerer. Table 7 summarizes the voltages of the EIBT and REMI electrodes, the electrodes are labelled according to the sketches in Appendix A. The ion beam was pulsed into a 10 µs bunch using one of the steerer electrodes located directly behind the source. The ion bunch was injected by lowering the voltage of "MIRROR1.2" to 0 for the first 60 µs after the bunch creation. The jet was operated at 4.5 bar upstream pressure.

Table 6: Ion source and beamline settings.

ion source settings	
kinetic energy	2 keV
focusing	1.1 kV
power	3.5 W (set) / 3.0 W (reading)
pressure	2.1×10^{-5} mbar
valve	2.3 V (ca 1 bar upstream)

ion source electrode stack	
electrode	voltage [V]
LENS	906
UP	0
DOWN	0
LEFT	75.1
RIGHT	3.6

90°-deflector	
electrode	voltage [V]
inner	-470.6
outer	539.1

Table 7: EIBT and REMI settings.

electrode	voltage [V]
MIRROR1.1	2676
MIRROR1.2	2228
MIRROR2	2622
LENS1	1796
LENS2	1853
UP1	32.2
RIGHT1	2.3
DOWN1	50.7
LEFT1	45.7
UP/LEFT2	4.6
DOWN/LEFT2	35.4
UP/RIGHT2	29.4
DOWN/RIGHT2	0
REMI1	-50
TUBE1	-50
GRID1	-50
REMI2	50
TUBE2	50
GRID2	50

C Experimental settings for the ion bunching

Table 8 lists the EIBT settings used for the presented RF-bunching test measurement. The labelling of the electrodes is according to the schemes in Appendix A. The bunching was performed by adding a sine signal of 7.5 V amplitude and 26.560 kHz frequency on the outermost exit side mirror electrode. The ions were produced with the previously used electron impact ion source, described in [26].

Table 8: EIBT settings in the bunching test.

electrode	voltage [V]
MIRROR1.1	3200
MIRROR1.2	2663
MIRROR2	3200
LENS0	2690
LENS1	2251
LENS2	2213
UP1	0
RIGHT1	0
DOWN1	0
LEFT1	0
UP/LEFT2	0
DOWN/LEFT2	7.8
UP/RIGHT2	0
DOWN/RIGHT2	0

References

[1] Wikimedia Commons. *Schematic drawing of an einzel lens*. 2017 (accessed: 12.08.23). URL: https://commons.wikimedia.org/wiki/File:Einzel_lens_schematic_drawing.svg.

[2] P. Cörlin. "Tracing ultra-fast molecular dynamics in O2+ and N2+ with XUV–IR pump–probe experiments". PhD thesis. Combined Faculty of Natural Sciences and Mathematics of the Ruperto-Carola-University of Heidelberg, 2015. DOI: 10.11588/heidok.00019644.

[3] Th. Ergler et al. "Spatiotemporal Imaging of Ultrafast Molecular Motion: Collapse and Revival of the D_2^+ Nuclear Wave Packet". In: *Phys. Rev. Lett.* 97 (19 2006), p. 193001. DOI: 10.1103/PhysRevLett.97.193001.

[4] D. Fischer. "Aufbau eines Reaktionsmikroskops zur Untersuchung von Ion-Atom-Stößen". Diploma thesis. University of Freiburg, 2000.

[5] Z. Fradkin et al. "Protein and peptide cross sections and mass spectra in an electrostatic ion beam trap". In: *Journal of Instrumentation* 12.05 (2017), P05008. DOI: 10.1088/1748-0221/12/05/P05008.

[6] M. W. Froese et al. "The decay of ion bunches in the self-bunching mode". In: *New Journal of Physics* 14.7 (2012), p. 073010. DOI: 10.1088/1367-2630/14/7/073010.

[7] R. K. Gangwar et al. "Autoresonance Cooling of Ions in an Electrostatic Ion Beam Trap". In: *Phys. Rev. Lett.* 119 (10 2017), p. 103202. DOI: 10.1103/PhysRevLett.119.103202.

[8] D. Gupta et al. "Time-dependent dynamics of radio-frequency-bunched ions in an electrostatic ion beam trap". In: *Phys. Rev. E* 107 (4 2023), p. 045202. DOI: 10.1103/PhysRevE.107.045202.

[9] C. C. Harper et al. "Accurate Sizing of Nanoparticles Using a High-Throughput Charge Detection Mass Spectrometer without Energy Selection". In: *ACS Nano* 17.8 (2023), pp. 7765–7774. ISSN: 1936-0851. DOI: 10.1021/acsnano.3c00539.

[10] R. Hegerberg, T. Stefansson, and M. T. Elford. "Measurement of the symmetric charge-exchange cross section in helium and argon in the impact energy range 1-10 keV". In: *Journal of Physics B: Atomic and Molecular Physics* 11.1 (1978), p. 133. DOI: 10.1088/0022-3700/11/1/017.

[11] A. Kramida et al. *NIST Atomic Spectra Database (version 5.10)*. National Institute of Standards and Technology, Gaithersburg, MD., 2022. DOI: 10.18434/T4W30F.

[12] A. Mahdian, A. Krükow, and J. Hecker Denschlag. "Direct observation of swap cooling in atom–ion collisions". In: *New Journal of Physics* 23.6 (2021), p. 065008. DOI: 10.1088/1367-2630/ac0575.

[13] R. Moshammer et al. "A 4 recoil-ion electron momentum analyzer: a high-resolution "microscope" for the investigation of the dynamics of atomic, molecular and nuclear reactions". In: *Nuclear Instruments and Methods in Physics Research Section B: Beam Interactions with Materials and Atoms* 108.4 (1996), pp. 425–445. ISSN: 0168-583X. DOI: https://doi.org/10.1016/0168-583X(95)01259-1.

[14] R. Moshammer et al. "Low-Energy Electrons and Their Dynamical Correlation with Recoil Ions for Single Ionization of Helium by Fast, Heavy-Ion Impact". In: *Phys. Rev. Lett.* 73 (25 1994), pp. 3371–3374. DOI: 10.1103/PhysRevLett.73.3371.

[15] G. A. Olah et al. "Chemical Aspects of Astrophysically Observed Extraterrestrial Methanol, Hydrocarbon Derivatives, and Ions". In: *Journal of the American Chemical Society* 138.5 (2016), pp. 1717–1722. DOI: 10.1021/jacs.6b00343.

[16] H. Pauly. *Atom, Molecule, and Cluster Beams I*. Berlin, Heidelberg: Springer, 2000. DOI: 10.1007/978-3-662-04213-7.

[17] A.V. Pavlov. "Ion Chemistry of the Ionosphere at E- and F-Region Altitudes: A Review". In: *Surv. Geophys.* 33 (2012), pp. 1133–1172. DOI: 10.1007/s10712-012-9189-8.

[18] H. B. Pedersen et al. "Ion Motion Synchronization in an Ion-Trap Resonator". In: *Phys. Rev. Lett.* 87 (5 2001), p. 055001. DOI: 10.1103/PhysRevLett.87.055001.

[19] M. Pitzer et al. “Direct Determination of Absolute Molecular Stereochemistry in Gas Phase by Coulomb Explosion Imaging”. In: *Science* 341.6150 (2013), pp. 1096–1100. DOI: 10.1126/science.1240362.

[20] T. Prohaska et al. “Standard atomic weights of the elements 2021 (IUPAC Technical Report)”. In: *Pure and Applied Chemistry* 94.5 (2022), pp. 573–600. DOI: 10.1515/pac-2019-0603.

[21] *RS-232 Interface Programmers Guide for NHQ High Precision and Standard Modules v2.1*. Germany: iseg Spezialelektronik GmbH, 2023. URL: https://iseg-hv.com/download/SYSTEMS/NIM/NHQ/iseg_manual_NHQ-RS-232-Programmers-Guide.pdf.

[22] H. T. Schmidt. “Electrostatic storage rings for atomic and molecular physics”. In: *Physica Scripta* 2015.T166 (2015), p. 014063. DOI: 10.1088/0031-8949/2015/T166/014063.

[23] L. Ph. H. Schmidt et al. “Spatial Imaging of the $\mathbf{H}_2{}^+$ Vibrational Wave Function at the Quantum Limit”. In: *Phys. Rev. Lett.* 108 (7 2012), p. 073202. DOI: 10.1103/PhysRevLett.108.073202.

[24] L. Ph. H. Schmidt et al. “Young-Type Interference in Collisions between Hydrogen Molecular Ions and Helium”. In: *Phys. Rev. Lett.* 101 (17 2008), p. 173202. DOI: 10.1103/PhysRevLett.101.173202.

[25] H. Schmidt-Böcking et al. “The COLTRIMS Reaction Microscope—The Spyhole into the Ultrafast Entangled Dynamics of Atomic and Molecular Systems”. In: *Annalen der Physik* 533.9 (2021), p. 2100134. DOI: 10.1002/andp.202100134.

[26] F. Schotsch. “TrapREMI - Development of a Reaction Microscope inside a Zajfman Trap and First Photodissociation Experiments on Stored Molecular Ions”. PhD thesis. Combined Faculty of Natural Sciences and Mathematics of the Ruperto-Carola-University of Heidelberg, 2021. DOI: 10.11588/heidok.00029402.

[27] F. Schotsch et al. “TrapREMI: A reaction microscope inside an electrostatic ion beam trap”. In: *Review of Scientific Instruments* 92.12 (2021), p. 123201. DOI: 10.1063/5.0065454.

[28] GSI Helmholtzzentrum für Schwerionenforschung GmbH. *The Go4 project page.* (accessed: 21.08.23). URL: https://www.gsi.de/en/work/research/experiment_electronics/data_processing/data_analysis/the_go4_home_page.

[29] G. Scoles, D. Bassi nad U. Buck, and D. Lainé. *Atomic and Molecular Beam Methods I.* New York, Oxford: Oxford University Press, 1988.

[30] Y. Toker et al. "The kick-out mass selection technique for ions stored in an Electrostatic Ion Beam Trap". In: *Journal of Instrumentation* 4.09 (2009), P09001. DOI: 10.1088/1748-0221/4/09/P09001.

[31] M. Unverzagt et al. "Collective Behavior of Electrons Emitted in Multiply Ionizing Collisions of 5.9 MeV/u U^{65+} with Ne". In: *Phys. Rev. Lett.* 76 (7 1996), pp. 1043–1046. DOI: 10.1103/PhysRevLett.76.1043.

[32] Polygon Physics webpage. *Technology: Ultracompact ultralow power ECR technology.* (accessed: 16.08.23). URL: https://polygonphysics.com/technology/ultracompact-ecr-technology/.

[33] Polygon Physics webpage. *TES: Single-cavity ECR-plasma based sources.* (accessed: 04.09.23). URL: https://polygonphysics.com/products/tes-multipurpose-ecr-source/.

[34] F. Werner et al. "Performance verification of the FlashCam prototype camera for the Cherenkov Telescope Array". In: *Nuclear Instruments and Methods in Physics Research Section A: Accelerators, Spectrometers, Detectors and Associated Equipment* 876 (2017). The 9th international workshop on Ring Imaging Cherenkov Detectors (RICH2016), pp. 31–34. ISSN: 0168-9002. DOI: https://doi.org/10.1016/j.nima.2016.12.056.

[35] J. L. Wiza. "Microchannel plate detectors". In: *Nuclear Instruments and Methods* 162.1 (1979), pp. 587–601. ISSN: 0029-554X. DOI: 10.1016/0029-554X(79)90734-1.

[36] D. Zajfman et al. "Electrostatic bottle for long-time storage of fast ion beams". In: *Phys. Rev. A* 55 (3 1997), R1577–R1580. DOI: 10.1103/PhysRevA.55.R1577.

[37] D. Zajfman et al. “High resolution mass spectrometry using a linear electrostatic ion beam trap”. In: *International Journal of Mass Spectrometry* 229.1 (2003). Mass Spectrometry Contributions to Nanosciences and Nanotechnology, pp. 55–60. ISSN: 1387-3806. DOI: 10.1016/S1387-3806(03)00255-0.

Danksagung

An dieser Stelle möchte ich mich bei allen bedanken, die mich bei der Fertigung dieser Arbeit auf die eine oder andere Weise unterstützt haben.

Als Erstes badanke ich mich herzlich bei meinem Betreuer Robert Moshammer sowie der gesamten Gruppe. Danke für die Möglichkeit, meine ersten Erfahrungen in der wissenschaftlichen Forschung durch die Arbeit in der Gruppe zu sammeln! Roberts anschauliche Erklärungen, erfahrungsbasierte Ratschläge sowie die ausführliche Diskussionen mit ihm waren sehr fördernd für das tiefere Verständnis der Materie und Entwickeln einer gewissen Intuition zum Lösen der auftretenden Probleme.

Besonderer Dank geht an Frans Schotsch, der den TrapREMI entwickelt und mir eine hervorragende Einführung in die Arbeit mit dem Aufbau noch vor dem Beginn dieser Masterarbeit gegeben hat.

Claus Dieter Schröter hat das Design für den Jet-Aufbau bereitgestellt. Seine Unterstützung mit Rat und Tat bei dem Aufbauen des Jets sowie bei allgemeinen Fragen im Bereich Vakuumtechnik waren extrem hilfreich.

Alexander von der Dellen hat mich umfangreich bei den Montagearbeiten unterstützt. Ohne seine technische Expertise und Handfertigkeit hätte die Montage wesentlich länger gedauert.

Florian Trost, Weiyu Zhang, Felix Herrmann und Cristian Medina haben mir bei der Korrektur dieser Arbeit geholfen. Danke Euch für die hilfreiche Diskussionen und Ratschläge!

Zuletzt möchte ich mich bei Thomas Pfeifer für erkentnissvolle und motivierende Gespräche sowie für das Schaffen einer produktiven und gemütlichen Atmosphäre in der Abteilung bedanken, welche den Austausch mit Mitmenschen sowie gegenseitige Unterstützung fördert.

Erklärung:

Ich versichere, dass ich diese Arbeit selbstständig verfasst habe und keine anderen als die angegebenen Quellen und Hilfsmittel benutzt habe.

Heidelberg, den 26.09.2023